

# Adiabatic melting experiment: ultra-low temperatures in helium mixtures

---

Tapio S. Riekki

# Adiabatic melting experiment: ultra-low temperatures in helium mixtures

**Tapio S. Riekki**

**Due to coronavirus pandemic this defence was postponed to be held on 25th September 2020.**

A doctoral dissertation completed for the degree of Doctor of Science (Technology) to be defended, with the permission of the Aalto University School of Science, at a public examination held at the lecture hall R003/F239a of the school on 17th April 2020 at 12.

**Aalto University  
School of Science  
Department of Applied Physics  
μKI group**

**Supervising professor**

Prof. Pertti Hakonen, Aalto University, Finland

**Thesis advisor**

Doc. Juha Tuoriniemi, Aalto University, Finland

**Preliminary examiners**

Prof. Kurt Gloos, University of Turku, Finland

Dr. Andrew Casey, Royal Holloway, United Kingdom

**Opponent**

Prof. Richard Haley, Lancaster University, United Kingdom

Aalto University publication series

**DOCTORAL DISSERTATIONS** 39/2020

© 2020 Tapio S. Riekkö

ISBN 978-952-60-8992-8 (printed)

ISBN 978-952-60-8993-5 (pdf)

ISSN 1799-4934 (printed)

ISSN 1799-4942 (pdf)

<http://urn.fi/URN:ISBN:978-952-60-8993-5>

Unigrafia Oy

Helsinki 2020

Finland



**Author**

Tapio S. Riekk

**Name of the doctoral dissertation**

Adiabatic melting experiment: ultra-low temperatures in helium mixtures

**Publisher** School of Science

**Unit** Department of Applied Physics

**Series** Aalto University publication series DOCTORAL DISSERTATIONS 39/2020

**Field of research** Engineering Physics, Physics

**Manuscript submitted** 17 December 2019

**Date of the defence** 17 April 2020

**Permission for public defence granted (date)** 6 February 2020

**Language** English

☐ **Monograph**

☒ **Article dissertation**

☐ **Essay dissertation**

**Abstract**

Mixture of the two stable helium isotopes,  $^3\text{He}$  and  $^4\text{He}$ , is a versatile system to study at low temperatures. It is a mixture of two fundamentally different quantum mechanical particles: fermions and bosons. Bosonic  $^4\text{He}$  component of the dilute mixture is known to become superfluid at about 2 K, while superfluidity of the dilute fermionic  $^3\text{He}$  component has not yet been observed. The transition is anticipated to occur at temperatures below 0.0001 K (i.e. 100  $\mu\text{K}$ ).

To reach such ultra-low temperatures, new cooling methods need to be developed, one of which is the main subject of this thesis. Current, well-established, cooling methods rely on external cooling, where a metallic coolant is used to decrease temperature in a liquid helium sample. Their performance is limited by rapidly increasing thermal boundary resistance.

Our novel adiabatic melting method relies on internal cooling process, where both the coolant and the sample are same helium. First, we create a phase-separation in the mixture by increasing its pressure to about 25 times the atmospheric pressure. This solidifies the  $^4\text{He}$  component, and we ideally end up with a system of pure solid  $^4\text{He}$  and pure liquid  $^3\text{He}$ . The phase-separated system is then precooled by conventional methods, after which the solid is melted. This allows  $^4\text{He}$  to mix with  $^3\text{He}$  again in heat absorbing process, resulting in a saturated mixture with about 8% molar  $^3\text{He}$  concentration. In theory, the mixing can reduce temperature by more than a factor 1000, but external heat leaks and imperfect phase-separation reduced this to the factor 5-7 in this work.

We study the performance of the melting method under various conditions, such as different melting rates, various total amount of  $^3\text{He}$ , and alternate configurations of the setup. We also developed a computational model of the system, which was needed to evaluate the lowest achieved temperatures, as the mechanical oscillators used for thermometry had already become insensitive. For it, we studied the thermal coupling parameters of our system, including thermal boundary resistances and  $^3\text{He}$  thermal conductivity. The lowest resolved temperature was  $(90 \pm 20) \mu\text{K}$ , still above the superfluid transition of the  $^3\text{He}$  component of the mixture. We also present suggestions for future improvements for the setup.

**Keywords** superfluid, helium-3, helium-4, helium mixture, adiabatic melting

**ISBN (printed)** 978-952-60-8992-8

**ISBN (pdf)** 978-952-60-8993-5

**ISSN (printed)** 1799-4934

**ISSN (pdf)** 1799-4942

**Location of publisher** Helsinki

**Location of printing** Helsinki **Year** 2020

**Pages** 191

**urn** <http://urn.fi/URN:ISBN:978-952-60-8993-5>



**Tekijä**

Tapio S. Riekkö

**Väitöskirjan nimi**

Adiabaattinen sulatuskoe: erittäin matalat lämpötilat heliumseoksissa

**Julkaisija** Perustieteiden korkeakoulu

**Yksikkö** Teknillisen fysiikan laitos

**Sarja** Aalto University publication series DOCTORAL DISSERTATIONS 39/2020

**Tutkimusala** Teknillinen fysiikka, fysiikka

**Käsikirjoituksen pvm** 17.12.2019

**Väitöspäivä** 17.04.2020

**Väittelyluvan myöntämispäivä** 06.02.2020

**Kieli** Englanti

☐ **Monografia**

☒ **Artikkeliväitöskirja**

☐ **Esseeväitöskirja**

**Tiivistelmä**

Kahden vakaan heliumisotoopin  $^3\text{He}$ :n ja  $^4\text{He}$ :n seos on monipuolinen tutkimuskohde matalissa lämpötiloissa. Se on kahden kvanttimekaanisen perushiukkas-tyypin eli fermionien ja bosonien seos. Bosoninen  $^4\text{He}$  -komponentti muuttuu tunnetusti supranesteeksi noin 2 K lämpötilassa, kun taas fermionisen  $^3\text{He}$ :n suprajuoksevuutta seoksessa ei ole vielä havaittu. Siihen tarvittavan lämpötilan on arvioitu olevan alle 0,0001 K (eli 100  $\mu\text{K}$ ).

Noin matalien lämpötilojen tavoittelu vaatii uusien jäähdytystapojen kehittämistä, joista yksi on tämän väitöskirjan aiheena. Tällä hetkellä käytetyt tekniikat perustuvat ulkoiseen jäähdyttämiseen, jossa kylmä metalli jäähdyttää nestemäistä heliumia. Tällöin ongelmaksi muodostuu terminen rajapintavastus, joka estää lämmön siirtymistä nesteen ja metallin välillä.

Adiabaattisessa sulatusmenetelmässä jäähdytys sen sijaan kohdistuu suoraan nestemäiseen heliumiin. Aluksi  $^3\text{He}$ - ja  $^4\text{He}$  -komponentit erotetaan nostamalla paine noin 25 kertaa normaaliin ilmanpaineeseen, jolloin  $^4\text{He}$  kiteytyy. Parhaassa tapauksessa näin saatu systeemi koostuu puhtaasta kiinteästä  $^4\text{He}$ :stä ja puhtaasta nestemäisestä  $^3\text{He}$ :sta. Seuraavaksi se jäähdytetään ulkoisilla menetelmillä, minkä jälkeen  $^4\text{He}$  kide sulatetaan. Tällöin se pystyy jälleen sekoittumaan  $^3\text{He}$ :n kanssa lämpöä sitoen muodostaen kylläisen seoksen, jossa on noin 8%  $^3\text{He}$ :a. Teoriassa näin on mahdollista alentaa lämpötilaa tekijällä yli 1000 mutta käytännössä ulkoiset lämpövuodot ja epätäydellinen isotooppien erottuminen rajoittivat sen tässä työssä tekijään noin 5-7.

Tutkimme adiabaattisen sulatusjäähdytyksen toimintaa erilaisissa olosuhteissa: vaihtelimme niin kiteen sulatusnopeutta,  $^3\text{He}$ :n kokonaismäärää kuin myös koejärjestelyn asetuksia. Kehitimme myös laskennallisen mallin järjestelmästäämme, jota tarvittiin lämpötilojen määrittämiseen, sillä lämpömittareina käyttämämme mekaaniset värähtelijät eivät enää olleet tarpeeksi herkkiä matalimmissa lämpötiloissa. Sitä varten tutkimme koejärjestelymme lämmönsiirtoparametreja, kuten rajapintavastuksia ja  $^3\text{He}$ :n lämmönjohtavuutta. Matalin arvioitu lämpötila oli  $(90 \pm 20) \mu\text{K}$ , joka oli yhä seoksessa olevan  $^3\text{He}$ :n suprajuoksevuuslämpötilan yläpuolella. Ehdotamme lopuksi myös parannuksia koejärjestelyyn.

**Avainsanat** supraneste, helium-3, helium-4, heliumseos, adiabaattinen sulatus

**ISBN (painettu)** 978-952-60-8992-8

**ISBN (pdf)** 978-952-60-8993-5

**ISSN (painettu)** 1799-4934

**ISSN (pdf)** 1799-4942

**Julkaisupaikka** Helsinki

**Painopaikka** Helsinki

**Vuosi** 2020

**Sivumäärä** 191

**urn** <http://urn.fi/URN:ISBN:978-952-60-8993-5>



# Contents

<b>Abstract</b>	<b>iii</b>
<b>Tiivistelmä</b>	<b>v</b>
<b>Contents</b>	<b>vii</b>
<b>Acknowledgments</b>	<b>ix</b>
<b>List of publications</b>	<b>xiii</b>
<b>Author's contribution</b>	<b>xiv</b>
<b>1 Introduction</b>	<b>1</b>
<b>2 Experimental setup</b>	<b>7</b>
2.1 Cooling system . . . . .	7
2.2 Cell . . . . .	8
2.3 Thermal gate . . . . .	10
2.4 Superleak line and the bellows system . . . . .	11
2.5 Quartz tuning fork . . . . .	14
2.5.1 Second sound anomalies . . . . .	16
2.6 Measurement procedure . . . . .	20
<b>3 Theory</b>	<b>23</b>
3.1 Thermodynamics of saturated $^3\text{He}$ – $^4\text{He}$ mixture . . . . .	23
3.2 Computational model . . . . .	28
<b>4 Results</b>	<b>33</b>
4.1 Quartz tuning forks at low temperatures . . . . .	34
4.1.1 Calibration . . . . .	37
4.1.2 Saturation in the response . . . . .	38
4.2 Kapitza resistances . . . . .	39
4.2.1 Plain cell wall . . . . .	40
4.2.2 Sinter . . . . .	41

---

4.3	Superfluid $^3\text{He}$ thermal conductivity . . . . .	45
4.4	Heat leaks . . . . .	50
4.5	Melts at higher temperatures . . . . .	54
4.5.1	Thermal gate operation . . . . .	55
4.5.2	Melting with the bellows system . . . . .	57
4.6	Lowest temperatures . . . . .	59
4.6.1	Simulations with altered melting conditions . . . . .	62
<b>5</b>	<b>Conclusions</b>	<b>67</b>
	<b>List of symbols</b>	<b>71</b>
	<b>References</b>	<b>75</b>

# Acknowledgments

The research presented in this thesis made use of the OtaNano - Low Temperature Laboratory infrastructure at the Aalto University School of Science. The work was partly supported by the Academy of Finland's Center of Excellence programme, and the EU-funded European Microkelvin Platform. Personal grants by the Jenny and Antti Wihuri Foundation, and travel support by the Magnus Ehrnrooth Foundation and by Aalto University's Education Network in Condensed Matter and Materials Physics are also acknowledged. I thank my supervisor Professor Pertti Hakonen for regular discussions about the current state of the experiment, as well as for making sure that all paperwork and practical aspects regarding pre-examination and preparation for the thesis defense went smoothly.

The adiabatic melting experiment, the development of a completely new cooling method, was a massive undertaking, and its success would not have been possible without the current members of the  $\mu$ KI-group, and the groundwork laid by the past members. I was truly fortunate to have been able to stand on the shoulders of giants.

The person that has influenced me the most was the leader of the  $\mu$ KI-group, and instructor to my thesis, Docent Juha Tuoriniemi. His guidance helped me gain better understanding in low temperature experimental techniques, numerical modeling, and, most importantly, the physics underlying the superfluid phenomena. He had the invaluable ability to give young graduate student enough freedom and responsibility to allow him to push his skills and gain some much-needed confidence, while at the same time always being available for support.

The mastermind behind the adiabatic melting experiment was Dr. Alexander Sebedash. The experiment would not have been possible without his efforts in turning it from an idea to reality. His knowledge in constructing low temperature experimental setups is truly unrivaled, and I learned a great deal from him during the hours we worked together installing the experiment to our cryostat.

When I joined the Low Temperature Laboratory in the summer of 2012, midst of my Bachelor's studies, I had virtually no experience in practical side of experimental physics. I am extremely grateful to Dr. Matti Manninen, then a graduate student in  $\mu$ KI, who took me under his wing and patiently guided me through basically everything, from proper soldering technique to material selections and circuit building, often having to explain things multiple times.

During the years in the lab, I have had the privilege of getting to know some fascinating personalities. One of them is Dr. Juho Rysti, whom I first knew as a graduate student in  $\mu$ KI, and later as a post-doc in our dear rival, the ROTA-group. Banter with him have been an endless source of entertainment, whether they have been about "temperature in the sun" or the unjust plot-twists in the latest Star Wars movie. He has been instrumental in refining my skills in the art of arguing (or *vänköäminen*). I also thank the leader of the ROTA-group Docent Vladimir Eltsov for very useful discussions that encouraged me to dive deeper into the theoretical side of helium physics. Next, I thank Dr. Jere Mäkinen, whose abstract mind and complex train of thought occasionally made me feel little dim. That, however, was perfectly balanced by his limping jokes that made mine feel ingenious in comparison. I also wish to thank Dr. Petri Heikkinen, for his laid-back attitude that started to slightly rub on me, Dr. Samuli Autti, for all the laughter he has forced upon me, and M.Sc. Timo Kamppinen for his bubbly personality that never fails to brighten my day.

Besides the lab's traditional Wednesday-sauna, we started a new regular event: Friday-night board-games that allowed people to socialize across various experimental groups. For a slightly introverted personality such as myself, these were invaluable opportunities to get to know people I might not have acquainted otherwise. Especially I wish to thank Dr. Ville Kaupila, Dr. Laure Mercier de Lépinay, Dr. Jorge Tiago Santos, M.Sc. Karthik Suresh, M.Sc. Matti Tomi, M.Sc. Marie-Melody Volard, and M.Sc. Alpo Välimaa for the engaging games and conversations we have had during them and say that I am truly going to *Miss!* you.

If I were to name each person that left an impression to me by name this section would go on forever, and you are probably not here for my musings, but are eager to jump in the actual science. So, I wish to thank all the wonderful people in the lab for making it feel like a second home. I will forever cherish the time I have spent there.

Journey from a farmboy in Suomussalmi to here and now has not been through a path well-trodden. A path I could not have walked without knowing that I had the full support of my wonderful family behind me. From the bottom of my heart: thank you.



## List of publications

This Thesis consists of an overview and the following publications.

- I** T. S. Riekki, A. P. Sebedash, and J. T. Tuoriniemi. *Performance of adiabatic melting as a method to pursue the lowest possible temperature in  $^3\text{He}$  and  $^3\text{He}$ - $^4\text{He}$  mixture at the  $^4\text{He}$  crystallization pressure.* 39 pages, arXiv:1911.06083 (2019) (submitted to the Journal of Low Temperature Physics).
- II** T. S. Riekki, J. T. Tuoriniemi, and A. P. Sebedash. *Thermal conductivity of superfluid  $^3\text{He}$ -B in a tubular channel down to  $0.1T_c$  at the  $^4\text{He}$  crystallization pressure.* arXiv:1907.05197 (2019) (accepted to the Journal of Low Temperature Physics).
- III** T. S. Riekki, A. P. Sebedash, and J. T. Tuoriniemi. *Thermodynamics of the adiabatic melting of solid  $^4\text{He}$  in liquid  $^3\text{He}$ .* Physical Review B **99**, 054502 (2019).  
DOI: 10.1103/PhysRevB.99.054502
- IV** T. S. Riekki, J. Rysti, J. T. Mäkinen, A. P. Sebedash, V. B. Eltsov, and J. T. Tuoriniemi. *Effects of  $^4\text{He}$  film on quartz tuning forks in  $^3\text{He}$  at ultra-low temperatures.* Journal of Low Temperature Physics, **196**, 73 (2019).  
DOI: 10.1007/s10909-018-02141-y
- V** A. Sebedash, S. Boldarev, T. Riekki, and J. Tuoriniemi. *Adiabatic Melting Experiment on Helium Mixtures: Status and Prospects.* Journal of Low Temperature Physics, **187**, 588 (2017).  
DOI: 10.1007/s10909-017-1755-5
- VI** T. S. Riekki, M. S. Manninen, and J. T. Tuoriniemi. *Decoupling of first sound from second sound in dilute  $^3\text{He}$ -superfluid  $^4\text{He}$  mixtures.* Physical Review B, **94**, 224514 (2016).  
DOI: 10.1103/PhysRevB.94.224514

Throughout the overview, the publications will be referred to by their Roman numerals.

## Author's contribution

The publications in this Thesis are results of team work of the  $\mu$ KI-group at the Low Temperature Laboratory of the Department of Applied Physics in Aalto University School of Science.

The majority of results presented in this Thesis (Publications **I-IV**) were obtained during one extended cooldown of the low-temperature apparatus from late 2017 to early 2019. During this time, the author was chiefly responsible for carrying out the measurements, and taking care of the day-to-day operations, maintenance and troubleshooting of the experimental setup. The author was also heavily involved in planning the measurement schedule, and coming up with ideas to optimize the performance of the novel cooling method. Most of the data-analysis was done by him, and he was the main author of the prepared publications, with shared main authorship in Publication **IV**.

Before the experimental run, the author was involved in installing and testing the cooling setup, which also included locating and fixing the leak problems that came up. Furthermore, the heat-exchanger volume of the experimental cell was designed and built by him. In Publication **V**, which was prepared during that time, the author had a lesser role in discussing about the results and commenting the manuscript.

The author was responsible for designing and constructing the experimental cell used for Publication **VI**. He also planned and performed the measurements, carried out data-analysis and wrote the publication.

# Chapter 1

## Introduction

The era of modern low temperature physics began in 1908 when Heike Kamerlingh Onnes managed to liquefy helium at 4.2 K [1]. He used it to cool various pure metals, such as mercury, tin and lead to discover that their electrical conductivity became immeasurably small at low temperature in a phenomenon nowadays known as superconductivity [2]. He also learned that liquid helium itself started to behave unexpectedly when it was cooled down further by decreasing its pressure. At 2.2 K its viscosity disappeared completely, and it even started to creep up the walls of its container against gravity. What he had discovered was the first superfluid. Superfluidity originates from quantum mechanical properties of matter, and thus cannot be understood by drawing analogies to classical physics. This makes superfluid helium rather a unique system, as it represents a macroscopic manifestation of a quantum mechanical phenomena.

Helium has two stable isotopes: common  $^4\text{He}$  that Onnes had available, and rare  $^3\text{He}$  which is obtained from certain nuclear reactions involving tritium. The nuclei of  $^4\text{He}$  atoms consist of two protons and two neutrons, while  $^3\text{He}$  atoms have one less neutron. At room temperature these two are indistinguishable, apart from their small mass difference, as both are chemically inert, colorless, odourless noble gases. However, due to this one neutron difference, in the realm of quantum physics they represent the opposite sides of the world;  $^4\text{He}$  is a boson and  $^3\text{He}$  a fermion. The difference manifests only at sufficiently low temperature. Superfluidity occurs when a macroscopic amount of particles start to occupy the single lowest possible quantum mechanical energy state. For bosonic  $^4\text{He}$  this happens at the mentioned 2.2 K temperature under saturated vapor pressure. This phenomenon is akin to Bose-Einstein condensation (BEC) [3, 4] of sparse gases. The difference is that, at best, about 10% of helium atoms occupy the ground state while in "true" BEC, all atoms can eventually occupy the

lowest energy state, provided that temperature is decreased enough.

Fermionic  $^3\text{He}$ , on the other hand, needs to obey the Pauli exclusion principle, which prevents any two identical fermi particles from occupying the same quantum mechanical state. Instead,  $^3\text{He}$  atoms form pairs, much like electrons do in metals at the onset of superconductivity. According to the BCS-theory [5], these "Cooper-pairs" behave like a boson and can undergo condensation-like phenomenon. The requirement for the pair-forming is an attractive interaction between the constituent particles. In liquid helium this extremely weak attraction is caused by the exchange of phonons (or collective vibration quanta) between helium atoms. Since this attraction is weak, it is easily masked by thermal motion, which is why temperature needs to be of order 0.001 K (1 mK) to enable the pair forming between  $^3\text{He}$  atoms and the transition to the superfluid state. A factor of thousand difference between the superfluid transition temperatures of bosonic  $^4\text{He}$  and fermionic  $^3\text{He}$  illustrates their different nature.

When we mix the two isotopes together, we gain access to a new system with various interesting properties. The mixture phase diagram is shown in Fig. 1.1 at the saturated vapor pressure (SVP), and at 25 bar, the crystallization pressure of  $^4\text{He}$ . The  $\lambda$ -line separates all normal mixture from normal fluid  $^3\text{He}$ –superfluid  $^4\text{He}$  mixture. If there is enough  $^3\text{He}$  present, the uniform mixture may separate into  $^3\text{He}$ -rich and  $^4\text{He}$ -rich phases below about 0.9 K. The  $^3\text{He}$ -rich phase will become 100%  $^3\text{He}$  at sufficiently low temperature (essentially below 0.1 K), while the  $^4\text{He}$ -rich phase will always contain a certain amount of  $^3\text{He}$  even down to the zero-temperature limit (7% at SVP, 8% at 25 bar) [6]. The finite solubility at absolute zero is an extraordinary property as mixtures of classical substances tend to separate completely as temperature is lowered. This feature enables the operation of dilution refrigerators in which  $^3\text{He}$  is continuously mixed with  $^4\text{He}$  to provide cooling due to the endothermic mixing process. The finite solubility is also the basis of the adiabatic melting method. Whereas a dilution refrigerator typically operates around 10 mK, the adiabatic melting method enables us to produce cooling at a hundred times lower temperature  $\sim 0.1$  mK.

From now on, we will refer to the  $^4\text{He}$ -rich phase of the phase-separated mixture simply as "mixture" or "mixture phase", since our experiment was performed at low enough temperature to consider the other phase to be pure  $^3\text{He}$ , so we practically had only one mixture phase present. We will also consider the mixture phase to always be at its saturation  $^3\text{He}$  concentration.

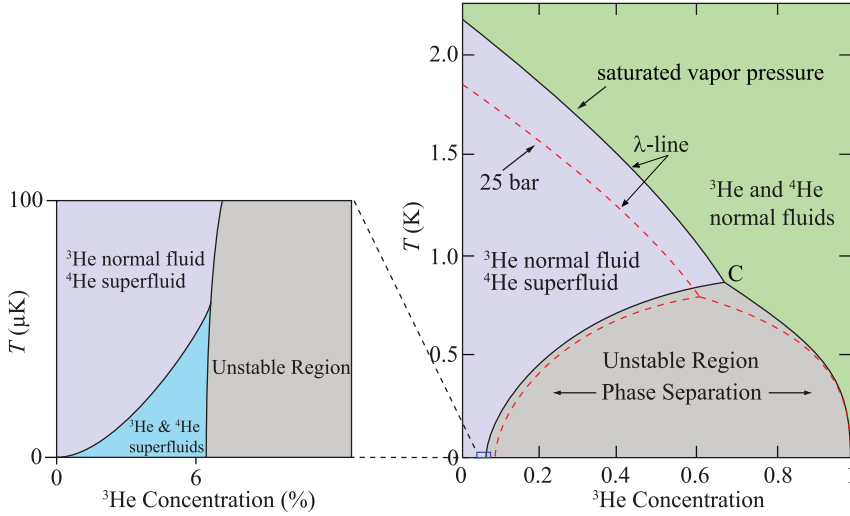


**Fig. 1.1** Phase diagram of  $^3\text{He}$ – $^4\text{He}$  mixture at saturated vapor pressure (essentially 0 bar below 0.3 K) and at 25 bar. The  $\lambda$ -line indicates the superfluid transition temperature of  $^4\text{He}$ . Above it both isotopes are in the normal state, while below it the  $^4\text{He}$  component is superfluid. Below the tricritical point C, within the unstable region, the mixture separates into  $^3\text{He}$ -rich and  $^4\text{He}$ -rich phases. The zoom-in figure shows the predicted behavior at ultra-low temperatures where the  $^3\text{He}$  component in the  $^4\text{He}$ -rich phase would become superfluid as well. [7]

The adiabatic melting method is based on phase-separation by solidification of the  $^4\text{He}$  component of the mixture. Unlike all other substances, helium does not solidify under its own saturated vapor pressure even at the zero-temperature limit. Instead, the pressure needs to be increased to about 25 bar (25 times normal air pressure) to force the formation of solid. This property is due to the large zero-point motion of the light helium atoms which prevents them from organizing into a crystalline lattice at lower pressures. Since  $^3\text{He}$  is lighter than  $^4\text{He}$ , its crystallization pressure is even higher, about 34 bar. When the pressure of the mixture is increased above the  $^4\text{He}$  crystallization pressure, at sufficiently low temperature, the forming solid  $^4\text{He}$  phase expels  $^3\text{He}$  atoms [8–10], and if the crystal is grown large enough, we can end up with a system of pure solid  $^4\text{He}$  and pure liquid  $^3\text{He}$ . When the solid is then allowed to melt,  $^4\text{He}$  is able to mix with  $^3\text{He}$  again producing cooling.

To attempt record-low temperatures, the system must be precooled be-

fore melting by other methods to absorb the heat released by the forced phase-separation and to produce appropriate initial conditions. Our setup used a combination of a dilution refrigerator and an adiabatic nuclear demagnetization cooler to get the initial temperature to about 0.5 mK. When temperature falls below  $T_c = 2.6$  mK [11], the pure  $^3\text{He}$  phase becomes superfluid, whose entropy decreases rapidly with temperature. Getting the entropy of the initial state as small as possible is critical, because the temperature after adiabatic melting is proportional to it.

The zoom-in feature of Fig. 1.1 illustrates the motivation behind our experiment: at some ultra-low temperature, the dilute  $^3\text{He}$  component of the mixture phase is anticipated to undergo a superfluid transition as well [12–16]. The attractive interaction that enables pair-forming between  $^3\text{He}$  atoms is further weakened by the presence of  $^4\text{He}$ , which suppresses the superfluid transition. Below about 100 mK,  $^4\text{He}$  is essentially in its quantum mechanical ground state, and thus basically an inert background that only modifies the interactions between  $^3\text{He}$  atoms. Rysti *et al.* [16] estimated that the highest temperature at which the dilute  $^3\text{He}$  component could become superfluid would be  $\sim 100\mu\text{K}$  at  $\sim 10$  bar pressure in saturated mixture. At 25 bar, the operational pressure of the melting method, it would be about  $40\mu\text{K}$ . Such a system would be a unique dense double-superfluid system consisting of bosonic and fermionic superfluids. Similar mixture superfluidity has been studied in sparse quantum gases [17–21], and observed in mixtures of  $^6\text{Li}$ – $^7\text{Li}$  [22], and  $^6\text{Li}$ – $^{174}\text{Yb}$  [23]. However, the interactions between the two superfluid species in them are significantly weaker than they would be in liquid helium system with  $10^4$  times the density.

To reach for temperatures below  $100\mu\text{K}$  in helium fluids is an extremely difficult undertaking. Already the search for the pure  $^3\text{He}$  superfluidity in the mK regime was an arduous task. It required development of new cooling methods such as the dilution refrigerator, and the Pomeranchuk cooling [24, 25] which utilizes solidification of  $^3\text{He}$  to absorb heat, until the new superfluid phase was discovered in the 1970s [26, 27]. Now, we find ourselves in a similar situation, as the current cooling methods are not able to cool the mixture enough to get to the superfluid mixture state. One of the best attempts was made by Oh *et al.* [28], who cooled helium mixture at 10 bar with an adiabatic nuclear demagnetization cryostat. Such a device is able to cool electrons in copper to far below 0.1 mK, but the problem arises from establishing good enough thermal contact between the copper coolant and liquid helium sample. As temperature is

lowered, thermal boundary resistance, known as the Kapitza resistance [29], between metals and liquid increases rapidly creating a bottleneck for cooling. The thermal contact can be improved by increasing the surface area between the coolant and liquid, usually by covering the surfaces with sintered metal powders. Oh *et al.* [28] reported that their cell had a surface area of about 4000 m<sup>2</sup>, and the lowest temperature achieved was 97  $\mu$ K. Increasing the surface area further becomes practically unviable as, for example, the relaxation of the <sup>3</sup>He concentration in the liquid trapped within the sinter will introduce additional sources of heating that further hampers the cooling of the sample.

The melting method circumvents the Kapitza bottleneck by relying on internal cooling: coolant and sample are the same helium. Kapitza resistance will only play a role in the precooling of the system. The experiment has been in development for about two decades [7, 30–34]. The previous experiment in 2007 [35] suffered from several technical difficulties that prevented thorough assessment of its performance. However, the principle of operation was found to be sound, and the lessons learned were implemented in the current iteration. In 2007, the sinter that was needed during precool, was placed in the same volume as solid <sup>4</sup>He causing too good a thermal connection to the precooler resulting in excessive heat load during the melting. We placed the sinter into a separate volume, and significantly reduced its amount to overcome this problem. Solid <sup>4</sup>He was grown and melted by using a superleak, which was a capillary filled with tightly packed metal-oxide powder. The flow impedance of such a line is so huge that only inviscid superfluid <sup>4</sup>He is able to flow through it at a meaningful rate ( $> 0.1 \mu\text{mol/s}$ ). The crystallization pressure in the porous material is slightly higher than in bulk, so the superleak line stays open even when there is a solid phase present in the open volume of the experimental cell. The flow rate is critically important as the cooling power of the melting process is directly proportional to it. In the previous experiment, the superleak was made of three sections with different materials, but this arrangement could only sustain about a half of the  $\sim 100 \mu\text{mol/s}$  flow that was required. In the current experiment, the superleak was made of two parts with a large buffer volume in between them, and the flow rates were significantly improved, as the new superleak was able to sustain up to  $600 \mu\text{mol/s}$  <sup>4</sup>He flow.

Thermometry at sub-100  $\mu$ K temperature is also extremely challenging. We used two quartz oscillators, one in the pure <sup>3</sup>He phase, the other in the mixture phase, to monitor the cell. They are small in size, easy

to install and use, and their operation does not produce excessive heating even at ultra-low temperatures. They do not need to be thermalized to liquid helium to probe its properties; the response of the oscillator changes according to the properties of its surrounding medium, irrespective of the temperature of the oscillator itself. The drawback is that their resonance response is not straightforward to convert to temperature due to the complex geometry of the oscillating body [36, 37], and complexities introduced by the presence of two different helium isotopes in our system. Furthermore, at the lowest temperatures of our experiment, the damping caused by the superfluid medium is expected to become significantly lower than the intrinsic damping of the oscillator, providing a limit for thermometry. In fact, we observed that this limit was reached earlier than anticipated which we attributed to the presence of superfluid  $^4\text{He}$  in the system. This is why a large part of this thesis involves constructing a computational model of the experimental arrangement to enable us to estimate the lowest temperatures achieved by the melting processes, which we were not able to measure directly.

## Organization of the overview

This thesis is organized as follows. We first go over the experimental setup, where we briefly describe the entire cooling system but focus on the low temperature parts. This is based on Publications **I** and **V**. We also discuss more about the quartz tuning fork oscillators in general, taking advantage of the results of Publication **VI**. Then, in the Theory chapter, we summarize the thermodynamic properties of  $^3\text{He}$ – $^4\text{He}$  mixtures as they relate to the adiabatic melting method, as well as describe the computational model of the system, that were discussed in Publications **II** and **III**. From there, we go on to present the key observations of our experiment. We begin by studying the quartz tuning fork behavior during the experiment using the results from Publication **IV**. Then, we analyze the various thermal connections in our system that were needed in constructing the computational model, followed by the estimations of the lowest temperatures. This part relies on the results presented in Publications **I** and **II**. In the final chapter we then summarize the thesis.

## Chapter 2

# Experimental setup

### 2.1 Cooling system

The goal of sub-100  $\mu\text{K}$  temperatures in helium places extreme demands on the performance of the entire cryostat. Each cooling stage needs to be especially stable to prevent any thermal fluctuations from causing excess heat load to the melting cell. The  $\mu\text{KI}$ -group cryostat has a tradition in setting record-low temperatures; in 1999 it managed to cool nuclear spins of rhodium down to 100 pK [38] by direct nuclear demagnetization as the final stage. Our cryostat performed the cooling in five stages.

- **Bath:** The cryostat was submerged in liquid  $^4\text{He}$ , vacuum isolated from the room temperature. This provided starting temperature of about 4 K.
- **Pot:** Some of the liquid in the bath was used to run a  $^4\text{He}$  evaporation cooler, or pot, which can reach temperatures down to about 1 K by continuously evaporating liquid helium. It cools the inner parts of the cryostat isolated from the bath by a second vacuum space. The pot arrangement had two volumes with separate flow impedances, but a common pumping line. One volume provided general cooling and was used to liquefy the incoming  $^3\text{He}$  needed for the next cooling stage, while the other provided thermal anchoring points for the capillaries connecting to the melting cell.
- **Dilution unit:** The dilution refrigerator continuously mixes  $^3\text{He}$  with  $^4\text{He}$  in a separate, isolated cycle to decrease the temperature to about 10 mK. The unit contains a mixing chamber and a still

from where  $^3\text{He}$  is evaporated by combination of heating and powerful pumps. The circulating  $^3\text{He}$  is recondensed by the 1 K pot and precooled by the outgoing helium flow from the mixing chamber to the still by large surface-area heat-exchangers.

- **Nuclear stage:** In adiabatic nuclear refrigerator, nuclear spins of copper are first aligned by a 9 T magnetic field, and precooled by the dilution unit. Then the two cooling units are thermally separated by an aluminum heat switch, after which the field is lowered adiabatically cooling the system to below 0.5 mK.
- **Melting cell** Solid  $^4\text{He}$  is melted, allowing it to mix with  $^3\text{He}$  to cool the mixture to below 0.5 mK (detailed description in the following Sections).

The first three units can be operated continuously, as long as the  $^4\text{He}$  bath is replenished regularly, providing a base temperature of around 10 mK for the experiment. The last two, however, must be operated cyclically. When the magnetic field of the nuclear stage is increased, the temperature temporarily goes up to about 50 mK, from which it is brought down by the dilution refrigerator in matter of 2-4 days. Then, the low-field state can be maintained for 1-2 weeks, depending on the desired temperature (0.2–1 mK). The lower the temperature, the lower the field is needed, where the external heat leaks limit the time that can be spent there. When the nuclear stage eventually becomes too warm, the field must once again be increased, bringing the temperature back to 50 mK, resetting the process. The temperature of the nuclear stage was measured by a pulsed platinum ( $^{195}\text{Pt}$ ) nuclear magnetic resonance measurement, or PLM. [39, 40]

Within the nuclear stage cycle, we operated the melting cell cycle that took about 1 day to grow and precool the crystal, and 10 min - 2 hours to melt the crystal, depending on the rate. In the optimal case, sub-100  $\mu\text{K}$  temperatures could be maintained during most of the melting time.

## 2.2 Cell

At the heart of the experimental setup, attached to the nuclear stage, was the melting cell, shown in Fig. 2.1. It was made of two separate volumes connected together by a channel that could be restricted by a pressure-operated cold-valve (thermal gate, TG), and had total volume  $(82 \pm 2) \text{ cm}^3$ .

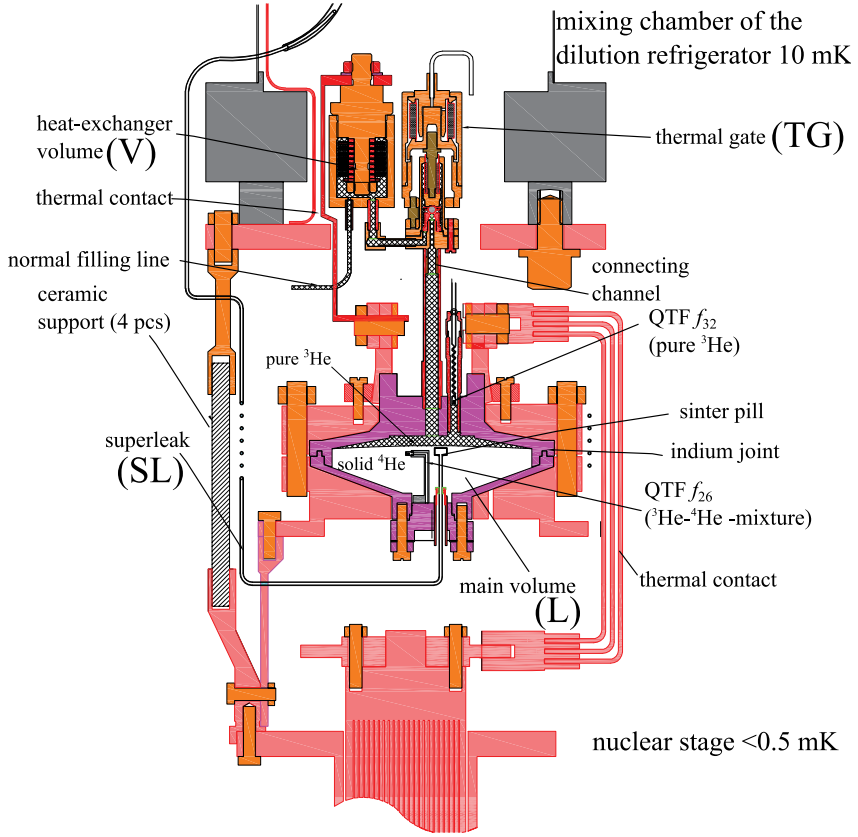


**Fig. 2.1** Schematic drawing of the low temperature parts of the experimental setup. The cell consists of a main volume (L) connected to a separate heat-exchanger volume (V) with a thermal gate (TG) in between. The walls of the cell are thermally connected to the nuclear stage. The superleak line (SL) leads to the bellows system shown in Fig. 2.2.

The main volume (L, 77 cm<sup>3</sup>) housed solid <sup>4</sup>He, liquid <sup>3</sup>He, and liquid <sup>3</sup>He–<sup>4</sup>He mixture at varying proportions, and was the coldest place of the entire experiment. At most, 90% of it was filled by solid. The smaller volume (V, 5 cm<sup>3</sup>) was a sinter-filled heat-exchanger volume, which provided thermal contact to the nuclear stage during the precooling. It and the connecting channel were mainly filled by liquid <sup>3</sup>He, with a small amount of mixture trapped in the porous sinter material.

The main volume was made of two high-purity copper shells encased between thick copper flanges to ensure that the structure could withstand 25 bar pressure. The inner shells were sealed by an indium joint, tightened by 16 bolts through the flanges. The heat-exchanger volume was also made of copper with a stack of 8 sintered discs tightly bolted to the lid of the volume. Each disc was covered by silver sinter on both sides, and the plates were separated by silver-coated copper spacers. The surface area of the stack was determined to be about 10 m<sup>2</sup>.

The setup had two filling lines for helium transport. A normal capillary line attached to the heat-exchanger volume was used to get <sup>3</sup>He into the system, while a superleak line attached to the bottom of the main volume allowed us to transfer superfluid <sup>4</sup>He to and from the cell to alter the amount of solid.

## 2.3 Thermal gate

The purpose of the thermal gate (TG) was to isolate the cell main volume from the heat-exchanger volume reducing the heat flow coming from the nuclear stage at times when the main volume was the coldest place of the experiment. This would make sure that we would not waste the cooling power of the melting process to cool the nuclear stage.

The thermal gate is a hydraulic needle valve, where the "needle" is a stainless steel ball at the end of a Vespel rod pressed against a conical copper saddle. The operation restricts the diameter of the channel connecting the two volumes of the experimental cell. The TG is operated by a miniature stainless steel bellows system with a brass framework and a copper bottom flange. The upper of the two bellows is connected to both a normal capillary and a superleak line, of which the former allows us to get <sup>3</sup>He into the volume, while the latter is used to change the pressure in the system via transfer of superfluid <sup>4</sup>He.

The TG operates in the pressure range 1-3 bar; at 1 bar it was completely open, while at 3 bar the ball was fully pressed against the saddle. The gate was not supposed to be superfluid  $^3\text{He}$  tight, but rather it needed to sufficiently reduce the transmission of  $^3\text{He}$  quasiparticles, that are responsible for the entropy transfer between the volumes.

## 2.4 Superleak line and the bellows system

Besides the main volume, the heat-exchanger volume and the thermal gate, the experimental setup also had a separate larger bellows system attached to the dilution unit of the cryostat, shown in Fig. 2.2. It was a thermal anchoring point to the superleak line, and provided an alternate method to operate the melting cell.

The superleak line was made of two parts: the first one started at the still of the dilution unit (0.7 K), and ended up at the lower bellows thermalized to the mixing chamber (10 mK), while the second one continued from the lower bellows to the main volume of the melting cell. A cylindrical sinter pill was attached to the cell-side end of the superleak, to prevent it from getting blocked by solid prematurely.

The bellows system was similar to the one in the thermal gate, except larger in size. The reason for this arrangement was to prevent possible fourth sound [41] modes generated in the upper (close to 1 K) parts of superleak from transmitting heat to the cell. Fourth sound can occur in porous materials, where the flow of normal fluid is restricted by the small open volume of the material, but inviscid superfluid can still flow freely. It can be generated by thermal fluctuations caused by unstable still temperature, or heat transferred due the flow of  $^4\text{He}$ , for example. It may then convert to ordinary sound (or first sound) causing heating at the low-temperature parts of the setup. With our arrangement, if any such sound is generated, most of its heat would be absorbed into the dilution unit from the lower bellows without ever reaching the main cell.

The thermal anchoring of the superleak to the still was made weak on purpose to keep it free from solid. The crystallization curve of  $^4\text{He}$  is flat at 25 bar up to about 1.5 K, after which the crystallization pressure starts to increase [42, 43]. Since the solid in the cell fixes the pressure, the point where the superleak line changes from a porous superleak to an ordinary capillary had to be warm enough to be free from solid and thus available for  $^4\text{He}$  transport. However, the thermalization was so weak that the upper

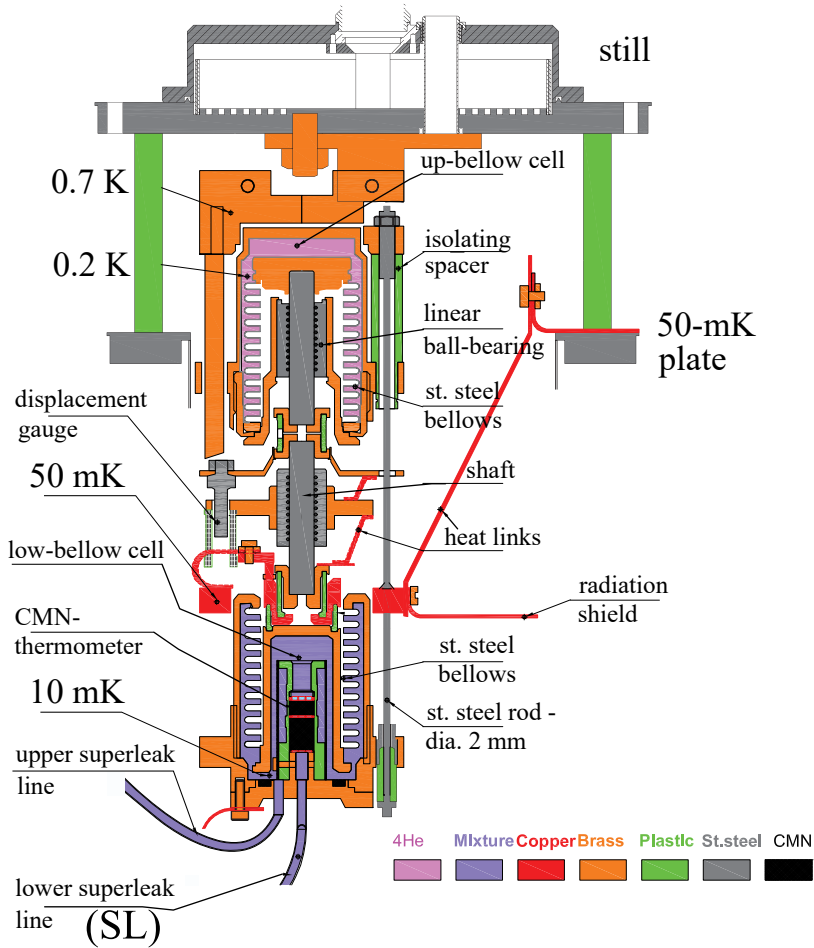


**Fig. 2.2** Schematic drawing of the bellows system placed within the dilution refrigerator. The lower superleak line (SL) connects to the melting cell (cf. Fig. 2.1).

end always remained free from solid unless we forced it to form there by significantly increasing the pressure in the line. The idea was to block the superleak by solid during precool to prevent heat leaks through it, but as things were, it was no longer easily achievable. We tried the forced-block method, but learned that the removal of the block would then cause a heating spike in the cell. Hence, the superleak line was kept mostly open during our experiment. Furthermore, we learned that the presence of the solid block had no significant influence on the observed heat leak to the melting cell. This may suggest that the heat transfer via fourth sound is not a valid concern at temperatures where there is practically no normal component in  $^4\text{He}$  ( $<100$  mK).

There were two ways to change the size of crystal in the main cell volume: directly from room temperature, or indirectly with the large bellows system. In the direct method, that we used the most,  $^4\text{He}$  was introduced from a gas bottle at room temperature, and pushed through a liquid nitrogen trap to the superleak line to grow the crystal. Then, to melt it, we pumped the same line from room temperature with a scroll pump, or if we were especially worried about heat leaks due to vibrations, simply to an empty volume. The amount of  $^4\text{He}$  transferred was measured by an in situ calibrated flowmeter. The flow measurement allowed us to calculate the amount of solid in the cell, since the transferred helium amount (in moles) and the change in solid size are related by a factor 10.5 [III]. This mode inherently had a connection between room temperature and the coldest parts of the experiment. Even though there were several thermalizations and buffer volumes along the way, there were concerns about the heat leak caused by this direct arrangement. This is why an alternative method by using the bellows system was devised.

The lower bellows was filled with saturated  $^3\text{He}$ – $^4\text{He}$  mixture at the mixing chamber temperature 10 mK, and it was thermally isolated from the upper bellows which was filled with pure liquid  $^4\text{He}$  at about 1 K. By changing the pressure in the upper bellows, the lower one could be compressed or depressed to cause flow from the bellows to the cell or vice versa. This way, the solid growth or melt would utilize only the lower part of the superleak, and thus be isolated from anything above 10 mK. Since the upper part of the superleak was no longer needed, it could be blocked by solid. The lower bellows had to be filled with saturated mixture to make sure that the nucleation of solid  $^4\text{He}$  would preferably occur in the cell main volume, and that there would be no large  $^3\text{He}$  concentration difference between the volumes to cause osmotic pressure driven flow. The areas of the bellows

were designed so that changing the upper bellows pressure between 10–25 bar would utilize its entire range of motion without risk of solid formation in the upper bellows volume. The temperature in the lower bellows was measured using a CMN-susceptibility thermometer. The performance of the thermal gate and the bellows will be discussed in Sections 4.5.1 and 4.5.2.

## 2.5 Quartz tuning fork

Quartz tuning forks (QTFs) are commercially produced piezoelectric oscillators that are commonly used as frequency standards in various devices, such as watches. When immersed in helium, they have been used to measure, temperature, pressure, concentration, viscosity or turbulence [44–49], for example. They are manufactured from a single-crystal quartz to a shape resembling an ordinary tuning fork. The two quantities extracted from a QTF measurement are typically the frequency at resonance, and its full-width at half-maximum (from now on referred to simply as "width").

The main volume of the experimental cell was monitored by two of these devices. A 32 kHz QTF (ECS-.327-8-14X, shown in Fig. 2.3) was placed in a tube on the top-half of the main volume, whereas a 26 kHz QTF (C-2 26.6670K-P:PBFREE) was in the middle of the main volume (see Fig. 2.1). The placements were chosen to have the first fork to always remain in liquid  $^3\text{He}$  phase to act as our main thermometer, while the second one was in place to monitor the properties of  $^3\text{He}$ – $^4\text{He}$  mixture. The mixture QTF was most of the time frozen in solid, only emerging partway through the melting process when the temperatures were at their lowest. The QTFs had different resonance frequencies to prevent them from interfering with each other.

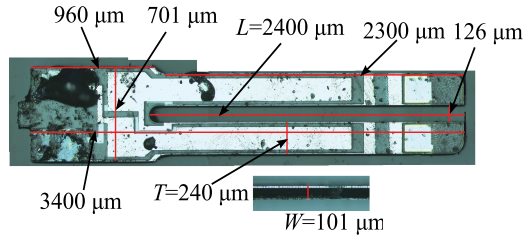


**Fig. 2.3** ECS-.327-8-14X quartz tuning fork with its dimensions.

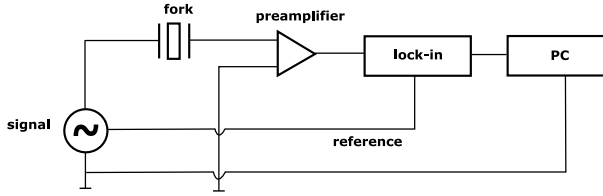


**Fig. 2.4** Circuit diagram for the QTF measurement.

QTFs were measured using a circuit illustrated in Fig. 2.4, where the excitation came from a signal generator and the output went first through a preamplifier before being read by a lock-in amplifier. The setup could be used either in a full-frequency sweep mode, or in a tracking mode. The tracking mode is based on operating the QTF in the linear regime (*i.e.* with sufficiently small excitation amplitude). In that case, we can assume that the resonance curve has a Lorentzian lineshape and that its area is constant. This means that a single measurement point is sufficient to evaluate both the resonance frequency and width [48]. The tracking mode is useful especially at small resonance widths, since it circumvents the need to wait a time proportional to the inverse-width after changing the frequency, which would be the case if we were doing a full-frequency sweep. The drawback of the tracking mode is that the lineshape of the resonance is lost. To utilize tracking, one must first determine the resonance curve parameters, as well as the background levels of the circuit, which then should not drift during the tracking measurement.

The temperature resolution of the QTF in  $^3\text{He}$  is based on observing the damping helium quasiparticles cause when they scatter from the surface of the QTF. Quasiparticles are collective excitations of the entire  $^3\text{He}$  ensemble whose mass differs from bare  $^3\text{He}$  mass. They are a more flexible way to describe certain many-body quantum phenomena, such as superfluidity. Other examples of quasiparticles would be electron-hole-pairs in semiconductors and phonons in crystalline solids.

In Fermi fluids, normal pure  $^3\text{He}$  or the  $^3\text{He}$  component of  $^3\text{He}$ - $^4\text{He}$  mixture in our case, the number of quasiparticles equals the number of bare atoms, and their mean-free path increases as  $T^{-2}$ . Eventually it becomes of the same order as the dimensions of the experimental cell, and fluid starts to behave like a gas of non-interacting (ballistic) particles [50, 51]. When the QTF is oscillating in the fluid, it transfers energy to helium, a part of which it receives back via the interactions between the quasiparti-

cles. Since the interactions decrease with decreasing temperature, so does this backscattering contribution. It results in increased energy loss from the oscillator observed as increasing resonance width as the temperature is lowered. Deep in the ballistic region, the backscattering contribution vanishes practically completely and the width saturates to a large value (order 100 Hz). This is exactly what happens in the mixture at low enough temperature, since the anticipated superfluid transition temperature  $40\ \mu\text{K}$  is far below the ballistic-crossover temperature.

The QTF response in pure  $^3\text{He}$  is different, because  $^3\text{He}$  becomes superfluid before the Fermi fluid mean-free path  $T^{-2}$  dependence brings it to the ballistic regime. Below the superfluid transition temperature  $T_c = 2.6\ \text{mK}$ , the number of quasiparticles starts to decrease exponentially, and the mean-free path of the remaining quasiparticles increases. Ultimately, we will reach the ballistic region in the pure  $^3\text{He}$  as well. But, the difference is that the decreasing number of quasiparticles reduces the energy loss from the QTF meaning that the observed width decreases with decreasing temperature, instead. When the damping by the quasiparticles becomes indistinguishable from the intrinsic damping of the QTF, or other temperature-independent damping mechanisms, the low temperature limit of thermometry in pure  $^3\text{He}$  is reached.

If the  $^3\text{He}$  component of  $^3\text{He}$ – $^4\text{He}$  mixture were to become superfluid, the width observed in mixture presumably would start to rapidly decrease, just like it does in pure  $^3\text{He}$ .

Besides detecting viscous damping, the QTFs can excite and sense second sound, or temperature waves, both in pure  $^4\text{He}$  and  $^3\text{He}$ – $^4\text{He}$  mixture. In mixture, they can also be considered as  $^3\text{He}$  concentration waves. They are prevalent at temperatures above 100 mK, where the proportions of normal and superfluid components are still changing. Below that,  $^4\text{He}$  is basically in its ground state and the mixture is normal fluid  $^3\text{He}$ –superfluid  $^4\text{He}$ . But, as we get closer to the superfluid transition temperature of  $^4\text{He}$  ( $T_\lambda = 2.17\ \text{K}$  in pure  $^4\text{He}$  at SVP),  $^4\text{He}$  starts to add to the normal fluid component. These temperatures are not extremely relevant to the melting experiment, but in the next section we will take a look at a peculiar phenomenon that occurs there.

### 2.5.1 Second sound anomalies

Superfluid can be understood macroscopically in terms of two-fluid model [52–54], in which the liquid consists of two (mostly) independent, but in-

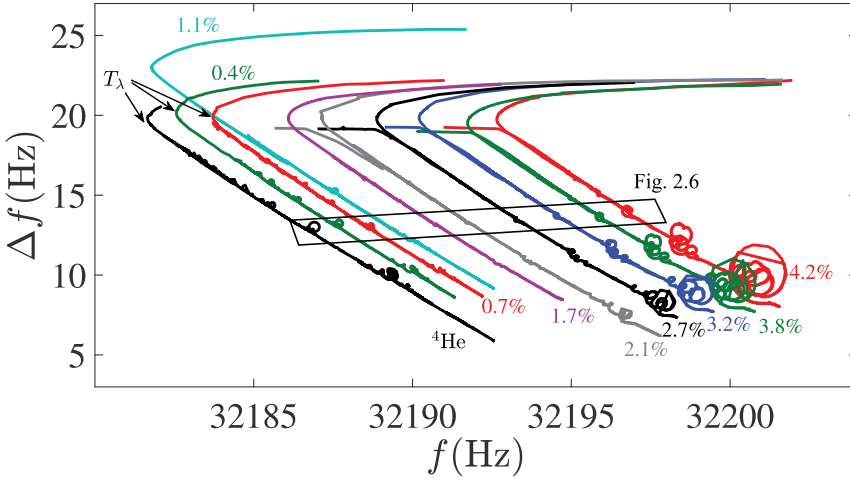


**Fig. 2.5** Resonance frequency versus resonance width of a QTF during the second sound measurement. Below the superfluid transition of  $^4\text{He}$   $T_\lambda$ , the anomalies caused by second sound appear as loops. The figure contains temperature sweeps both down and up, basically falling on top of each other. The 1.1% dataset was shifted due to some unreproducible reason, possibly related to impurities freezing on the surface of the fork. The framed region (along with the shifted 1.1% data) is the focus of Fig. 2.6.

separable, components: superfluid that is inviscid and has no entropy, and normal fluid that behaves like any ordinary fluid with finite viscosity and capability to transfer entropy. Various sound modes in superfluid medium can be then considered as different oscillation modes of these two intermingled fluids.

Bulk superfluid helium can support two sound modes: first sound is an ordinary pressure wave, while second sound is a temperature wave [55]. In first sound, superfluid and normal fluid component oscillate in phase, whilst in second sound, they oscillate in antiphase, resulting in entropy (and thus temperature) fluctuations at a constant pressure. Since  $^3\text{He}$  in the isotope mixtures is part of the normal fluid component, second sound in mixtures can also be interpreted as a  $^3\text{He}$  concentration wave.

The two sound modes are not usually independent, but rather they are coupled together. In pure  $^4\text{He}$  the coupling is solely through the thermal expansion coefficient. In  $^3\text{He}$ – $^4\text{He}$  mixture the coupling is modified since the density of the fluid now varies along with the fluctuating  $^3\text{He}$  concentra-

tion. At certain temperatures and concentrations, these contributions can cancel each other out, decoupling first sound from second sound [7, 56]. The coupling from second  $\rightarrow$  first, and first  $\rightarrow$  second is asymmetric: whereas second sound can decouple from first sound, first sound is always coupled to second sound.

The detection of second sound with quartz tuning forks is based on the mode's coupling to the first sound. QTF may generate second sound, but cannot directly measure it, since temperature oscillations do not cause a piezoelectric response. But, second sound can drive first sound via the coupling. This driven first sound can be detected by the QTF and it has the same waveform as the second sound driving it. The second sound mode can be generated directly by the fork, or it can come about from the first sound created by the fork via sound conversion.

The wavelength of second sound matches the characteristic dimensions (cf. Fig. 2.3) of a typical QTF. They can thus form standing waves within the dimensions of the QTF, which is observed as an anomaly in the resonance response. When the QTF response is plotted in frequency–width graph, these anomalies appear as loops [57–59], and their magnitude is an indicator of the sound coupling strength. Examples of the behaviors of such anomalies as a function of  $^3\text{He}$  concentration are shown in Figs. 2.5 and 2.6. The anomalies are clearly observable both in pure  $^4\text{He}$  and 4.2% mixture, but in between, at about 2% concentration, they almost vanish. Note, that even if the shape of the anomalies change due to the increasing  $^3\text{He}$  concentration and the increasing temperature relative to the  $T_\lambda$ , we can still identify corresponding features by focusing on their sequence of appearance: a larger anomaly preceded and followed by a smaller anomaly in the example of Fig. 2.6.

This demonstrates that there exists a region where first sound and second sound are extremely weakly coupled, and possibly even completely decoupled, provided that the  $^3\text{He}$  concentration is exactly right. When that happens, the standing second sound mode around the fork still exists, but it no longer drives the first sound that is ultimately responsible for the anomaly observed on the fork response. Since the standing waves occur only at very specific temperatures and concentrations, they can be used as reference points in temperature, assuming that the dimensions of the oscillator are known. But, as we have seen, there is a regime where they are not usable due to the decoupling phenomenon.

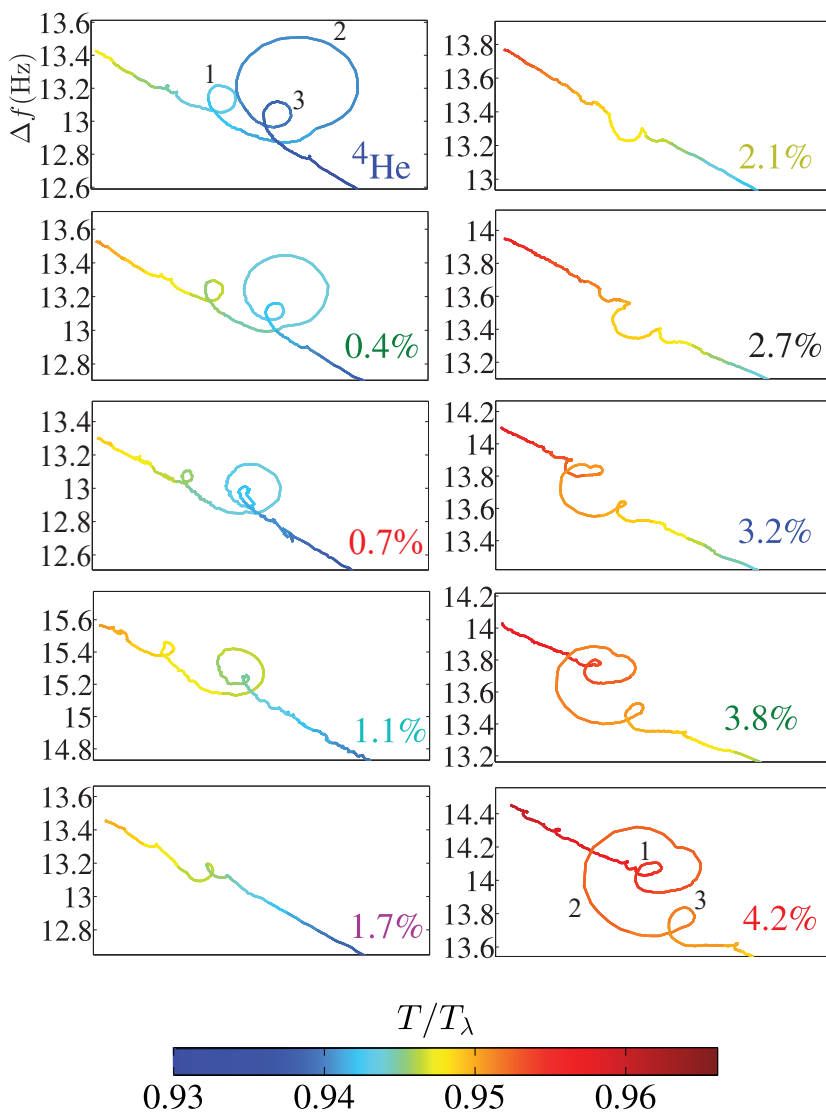


**Fig. 2.6** Close-up view of selected second sound anomalies from Fig. 2.5 (along with the shifted 1.1% data) followed through the decoupling region. The  $^3\text{He}$  concentration ranged from 0 to 4.2%, and the temperature is indicated by the color of the line. Equivalent anomalies, labeled 1–3, can be traced through different concentrations.

## 2.6 Measurement procedure

Now we shall return to the adiabatic melting experiment and take a look at a typical procedure in operating the melting cell. The approach described here aimed to achieve as low temperature as possible.

When the previous cooling stages were working, the next thing in order was to nucleate a solid  $^4\text{He}$  crystal in the experimental cell. That needed to take place at temperature below 50 mK to prevent  $^3\text{He}$  impurities from entering the solid phase [8–10]. During precooling, any such inclusion would not be properly thermalized to the bulk liquid in the cell and would thus remain at an elevated temperature. When solid is melted, these hot  $^3\text{He}$  bubbles would be released from solid heating up the system at a time most critical.

To nucleate the crystal, we increased pressure in the main volume of the cell by pushing  $^4\text{He}$  through the superleak line. The nucleation would preferably take place in the cell, since it was colder than the lower bellows, plus the cell main volume had a grafoil strip on the bottom to act as a nucleation site [60]. Even gravity would in principle assist in nucleations, since the melting cell resided underneath the bellows.

But, as often is the case in experimental physics, the reality was not so straightforward. There was clear randomness in the favored nucleation location; sometimes it occurred in the cell, as intended, but more often it tended to take place in the bellows volume, and occasionally even at the upper end of the superleak. Initially we suspected that  $^3\text{He}$ – $^4\text{He}$  mixture in the bellows was not saturated, which would reduce its crystallization pressure. But since adding more  $^3\text{He}$  there did not improve the situation, that was clearly not the case. We even tried to bombard the cell main volume with neutrons from a weak radiation source to provide a disturbance required for the nucleation to occur, but with no improvement. In the end the only way to guarantee nucleation in the cell was to heat the bellows volume significantly. A situation where the bellows was at around 200 mK, while the cell was still at about 2 mK saw the solidification to reliably happen where it was intended. Even then, the pressure had to be increased hundreds of millibars above the equilibrium crystallization pressure value before the nucleation actually took place. In principle, just a few millibars should have been sufficient. The origin of such high nucleation barrier is not understood.

As such, we decided to carry out the experiment with as few fresh nucleations as possible. This would result in increased inaccuracy in the es-

timated solid  $^4\text{He}$  amount, as the error in the flow measurement used to determine the crystal size would keep accumulating until a reset to zero when the entire crystal was gone.

After nucleation, the crystal was grown to the maximal size and the nuclear stage was magnetized, warming up the cell near to 50 mK. The nuclear stage was precooled with the dilution refrigerator to 10–12 mK, after which the two coolers were disconnected by the heat switch, and the nuclear stage was demagnetized to carry on the melting cell precool.

Since the magnetization of the nuclear stage heated the cell near to 50 mK, we decided to melt and regrow the crystal when the cell had cooled to below the pure  $^3\text{He}$  superfluid transition temperature  $T_c$ . With this procedure at no point we observed, or had a reason to suspect,  $^3\text{He}$  inclusions in the solid.

Now, for as long as the nuclear stage was capable to sustain  $<0.5$  mK temperatures, the standard of activity was as follows.

- **Precool:** After the final solid growth, the cell was allowed to cool towards as low temperature as possible, with goal being below 0.5 mK, corresponding to the  $^3\text{He}$  QTF width of about 10 Hz. This was allowed to happen as undisturbed as possible to observe the relaxation time towards the lower temperatures that would be an indicator of heat capacities and thermal contacts in the system. (1- 3 days)
- **Melt preparation:** As the ultimate precooling temperature was close, we periodically allowed a small flow out of the superleak line to ensure that the cell-side end was not partially blocked by solid. Had that been the case, melt initiation would have caused an unwanted heating spike. Also, at this point, the  $^3\text{He}$  QTF was switched from the full-frequency sweeps to the tracking mode with newly determined background parameters. The excitation amplitude was made as small as possible to prevent excess heating at the forthcoming ultra-low temperatures. ( $\sim 2$  h)
- **Melt:** The outward flow of the superleak was slowly increased, while keeping an eye on any odd heatings that would abort the operation. The chosen maximal flow was kept until about 80% of the solid was melted, after which the flow was slowly reduced back toward zero. At the end, we left a small outward flow in place to prevent the pressure and temperature gradient in the upmost parts of the capillaries from

pushing  $^4\text{He}$  back to the cell, regrowing the solid and causing heating. At about halfway of the melt, the mixture QTF was released from the solid, and it was measured by narrow full-frequency sweeps, or by the tracking mode. (10 min – 2 h)

- **Warm-up:** Post-melting warm-up period was observed long enough to ascertain the temperature the main volume relaxes towards, and at what rate. The small outward flow was maintained for 1-2 hours, until the pressure in the upper-end of the superleak line had stabilized. (6–12 h)
- **Regrowth:** Finally, the crystal would be regrown again and the cycle could be repeated. (8–12 h)

If at the regrowth period, the nuclear stage was becoming too warm, a new magnetization was necessary, warming the setup back to 50 mK.

Besides the procedure described above, we performed several diagnostic melts at higher temperatures to study the melting cell behavior, and the thermal couplings of the system. In those cases, it was not critical that the crystal had always been below the  $T_c$ , and the undisturbed precool and lengthy warm-up observation were not always necessary either.

## Chapter 3

### Theory

In this chapter we first go over the most important thermodynamical properties of  $^3\text{He}$ – $^4\text{He}$  mixture and pure  $^3\text{He}$  at the crystallization pressure of  $^4\text{He}$  25.64 bar [11]. We focus on their low-temperature properties ( $<10$  mK), and we are especially interested in their heat capacity and entropy which are involved in determining the performance of the melting process. After that, we will describe the computational model of the melting cell that was required to understand its behavior at the lowest temperatures, when the QTF thermometer had become insensitive.

#### 3.1 Thermodynamics of saturated $^3\text{He}$ – $^4\text{He}$ mixture

The phases present are pure  $^3\text{He}$ , dilute  $^3\text{He}$ – $^4\text{He}$  mixture at saturation molar  $^3\text{He}$  concentration  $x = 8.1\%$  [46], and solid phase that can be assumed to be pure  $^4\text{He}$ . The presence of the pure  $^3\text{He}$  phase ensures that the mixture remains always at saturation, while the solid fixes the pressure. Thus, we have a univariant three-phase system, where temperature  $T$  is the only free thermodynamic parameter. We begin by analyzing the heat capacities of various phases, which are measurable quantities, but then convert them to entropy, since through it we can better explain the principle of the cooling by the melting process.

Normal fluid  $^3\text{He}$  and mixture are deeply degenerate Fermi systems, meaning that their heat capacity is directly proportional to temperature. Mixture maintains this linear dependence down to sub-100  $\mu\text{K}$  temperatures, while at the  $T_c = 2.6$  mK, pure  $^3\text{He}$  heat capacity suddenly increases and then drops exponentially going towards lower temperatures [6, 61].

Furthermore, at  $T_{AB} = 0.917T_c \approx 2.4$  mK, pure  $^3\text{He}$  undergoes a second-order phase transition from superfluid A-phase to B-phase. But since the heat capacity during it is continuous, the transition does not affect the thermodynamic properties discussed here.

The linear temperature dependence of the mixture heat capacity means that it becomes the main contributor to the total heat capacity of the system at sufficiently low temperature. Compared to that, we can ignore phononic contributions to the heat capacity, in particular, the heat capacity of solid  $^4\text{He}$  can be assumed to be zero.

The heat capacity for  $n$  moles of degenerate Fermi fluid is given by

$$\frac{C}{nR} = \frac{\pi^2}{2} \frac{T}{T_F}, \quad (3.1)$$

where  $R$  is the molar gas constant and  $T_F$  is the Fermi temperature, which for pure  $^3\text{He}$  is  $T_{F,3} = 1.44$  K [62], and  $T_{F,m} = 0.38$  K for the isotope mixture.

The mixture Fermi temperature was evaluated from

$$T_{F,m} = \frac{\hbar^2}{2m^*k_B} \left( \frac{3\pi^2 N_A x}{V_m} \right)^{2/3}. \quad (3.2)$$

Here  $\hbar$ ,  $k_B$ , and  $N_A$  are the reduced Planck constant, Boltzmann constant, and Avogadro constant, respectively,  $m^* = 3.32m_3$  [16] is the effective mass of a  $^3\text{He}$  atom in mixture ( $m_3 = 3.0160293$  u is the bare  $^3\text{He}$  mass).  $V_m = V_{4,l}(1 + \alpha x)$  [13] is the molar volume of the mixture, which is the molar volume of liquid  $^4\text{He}$   $V_{4,l} = 23.16$  cm<sup>3</sup>/mol [63], modified by the additional space taken by the lighter  $^3\text{He}$  atoms, represented by the BBP-parameter  $\alpha = 0.164$  [13, 64]. Moreover, the molar volumes for the remaining two phases were  $V_3 = 26.26$  cm<sup>3</sup>/mol for pure  $^3\text{He}$  [65], and  $V_{4,s} = 20.97$  cm<sup>3</sup>/mol for solid  $^4\text{He}$  [66].

For the heat capacity of superfluid  $^3\text{He}$ , we used a phenomenological formula fitted to the experimental data by Greywall [67]

$$\frac{C_3}{n_3 R} \Big|_{T \leq T_c} = \frac{\pi^2 T_c}{2T_{F,3}} \left\{ \left[ A \left( \frac{T}{T_c} \right)^{-1} + B \left( \frac{T}{T_c} \right)^2 \right] \exp \left( -\frac{\Delta_0}{T} \right) \right\}, \quad (3.3)$$

where  $n_3$  is the amount of  $^3\text{He}$  (in moles),  $A = 8.242$  and  $B = 11.22$  are the fitting parameters, and  $\Delta_0 = 1.91T_c$  is the superfluid  $^3\text{He}$  energy gap at the zero-temperature limit, taken as average of the values given by Refs. [49] and [68].

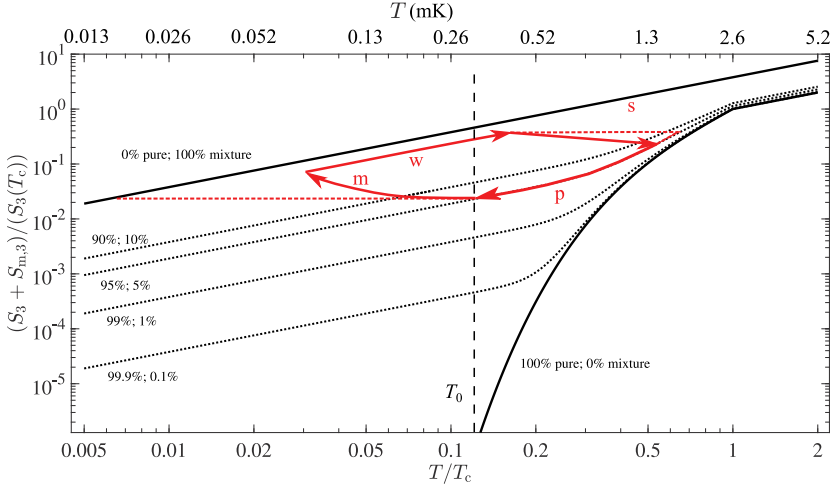


**Fig. 3.1** Entropies for various partitions of pure  $^3\text{He}$  and saturated  $^3\text{He}$ – $^4\text{He}$  mixture, per mole of  $^3\text{He}$  as a function of temperature relative to the pure  $^3\text{He}$  superfluid transition temperature  $T_c$ . Entropies are scaled by its value at the pure  $^3\text{He}$   $T_c$ . The percentages indicate how the total amount of  $^3\text{He}$  is split between the pure and the mixture phases. Red lines illustrate the operational cycle of the melting cell, with precooling temperature  $T_0$ , while the dashed red lines indicate ideal adiabatic behavior, for comparison. The labels correspond to (p) precool, (m) melt, (w) warm-up, and (s) solidification.

To illustrate the importance of the different temperature dependence below the  $T_c$  between mixture and pure  $^3\text{He}$ , we next convert heat capacities to entropy through the relation  $S = \int_0^T \frac{C}{T'} dT'$  ( $S_3$  and  $S_{m,3}$  are entropies per mole of  $^3\text{He}$  for pure and mixture phase, respectively). The result is shown in Fig. 3.1, where we have taken a fixed amount of  $^3\text{He}$ , and split it between the pure phase and the saturated mixture phase at various partitions. Since the entropy of pure  $^3\text{He}$  falls exponentially below the  $T_c$ , while the linear dependence is maintained in mixture, mixture will, even at very small quantities, dominate the total entropy of the system below approximately  $0.2T_c$ .

Figure 3.1 also has the operational cycle of the melting experiment drawn out. We begin by following the precool (p) curve. In the ideal case, this would correspond to the pure  $^3\text{He}$  curve, as all  $^4\text{He}$  would be in the solid phase, but in reality there will inevitably be some small amount of mixture left. As such, the total entropy of the system will eventually de-

crease only as  $\propto T$ . Then, as the desired precooling temperature  $T_0$  has been reached, the melting is initiated. In the perfectly adiabatic case, we would move horizontally from the initial curve towards the mixture curve. But again, since in reality there are always losses that bring additional entropy to the system (such as external heat leak), the actual melting curve (m) will instead bend upward, leaving us at elevated temperature. Since the actual system has a slight excess amount of  $^3\text{He}$ , there will always be pure  $^3\text{He}$  present, even if the entire crystal were melted. Therefore, at the end of the melt we do not reach the mixture-only curve. After melting, the warm-up (w) curve then follows parallel to the mixture curve toward higher temperatures. Finally, when the system reaches the initial temperature  $T_0$  again, the solid phase is regrown (s). Now we will not follow the adiabatic curve either, since the thermal contact to the nuclear stage already starts the precooling process during crystal growth, extracting entropy from the system.

If the initial state were to contain only pure  $^3\text{He}$  and solid  $^4\text{He}$ , we could decrease the after-melting temperature exponentially with precooling temperature. But, due to the presence of mixture, below about  $0.2T_c$ , we can only decrease the ultimate temperature in proportion to the initial temperature. The ratio between initial and final temperature is proportional to the ratio of initial and final state entropies. If we assume that the pure  $^3\text{He}$  entropy is negligible compared to the mixture, and ignore the heat leaks, it will simply become proportional to the amount of  $^3\text{He}$  in the mixture phase  $n_{m,3}$

$$\left( \frac{T_0}{T_{\text{final}}} \right)_{\text{max}} = \frac{(n_3 + n_{m,3})}{n_{m,3}}. \quad (3.4)$$

The cooling power of the melting process, on the other hand, is proportional to the difference between mixture and pure  $^3\text{He}$  entropy

$$\dot{Q}_{\text{melt}} = T \dot{n}_3 (S_{m,3} - S_3), \quad (3.5)$$

where a dot above a symbol indicates time derivative, and thus  $\dot{n}_3$ , is the rate at which  $^3\text{He}$  is transferred between the phases. Again, below  $0.2T_c$ , we can ignore the minuscule pure  $^3\text{He}$  entropy to get an expression with a numerical prefactor

$$\dot{Q}_{\text{melt}} \approx 109 \frac{\text{J}}{\text{mol K}^2} \dot{n}_3 T^2, \quad (3.6)$$

also displaying the squared temperature dependence. At  $T = 100\mu\text{K}$  with  $\dot{n}_3 = 100\mu\text{mol/s}$  we get about 100 pW of cooling power.

As discussed in Chapter 2, since we melt and grow the crystal via the superleak, we cannot directly control, or detect, the phase-transfer rate  $\dot{n}_3$ , but rather we control the  $^4\text{He}$  extraction rate  $\dot{n}_4$ . The connection between these two can be deduced as follows. Let us assume an infinitesimal amount of solid  $^4\text{He}$  is melted (or grown) resulting in a small change in the total solid  $n_s$ , pure  $^3\text{He}$   $n_3$ , and mixture amounts  $n_m$  (note that  $n_m$  is the total mixture amount, while  $n_{m,3}$  was the amount of  $^3\text{He}$  in mixture,  $n_{m,3} = xn_m$ )

$$v = (n_3 - \text{d}n_3)V_3 + (n_s - \text{d}n_s)V_{4,s} + (n_m + \text{d}n_m)V_m, \quad (3.7)$$

where  $v$  is the total volume of the cell. Next, we take the time derivative, and note that while  $^3\text{He}$  swaps phases its total amount stays constant  $\dot{n}_3 - x\dot{n}_m = 0$ , but the  $^4\text{He}$  amount is changed by the extracted amount  $\dot{n}_s - (1-x)\dot{n}_m = \dot{n}_4$ , thus yielding

$$\begin{aligned} \dot{n}_3 V_3 + \left[ \dot{n}_4 + (1-x) \frac{\dot{n}_3}{x} \right] V_{4,s} - \dot{n}_3 V_m &= 0 \\ \Leftrightarrow \dot{n}_3 &= \frac{x V_{4,s}}{(1+\alpha x) V_{4,l} - x V_3 - (1-x) V_{4,s}} \dot{n}_4, \end{aligned} \quad (3.8)$$

where the prefactor of  $\dot{n}_4$  gets a numerical value of 0.84. Hence, the low temperature cooling power of the melting process in terms of extracted  $^4\text{He}$  becomes,

$$\dot{Q}_{\text{melt},2} = 91 \frac{\text{J}}{\text{mol K}^2} \dot{n}_4 T^2. \quad (3.9)$$

Another useful factor that can be extracted from Eq. (3.7), by eliminating  $n_3$  and  $n_m$ , is the change in the amount of solid per extracted  $^4\text{He}$ :

$$\dot{n}_s = \left[ 1 + \left( 1 - \frac{1}{x} \right) \frac{x V_{4,s}}{(1+\alpha x) V_{4,l} - x V_3 - (1-x) V_{4,s}} \right] \dot{n}_4 \approx 10.5 \dot{n}_4 \quad (3.10)$$

useful in keeping track of the amount of solid in the experimental cell.

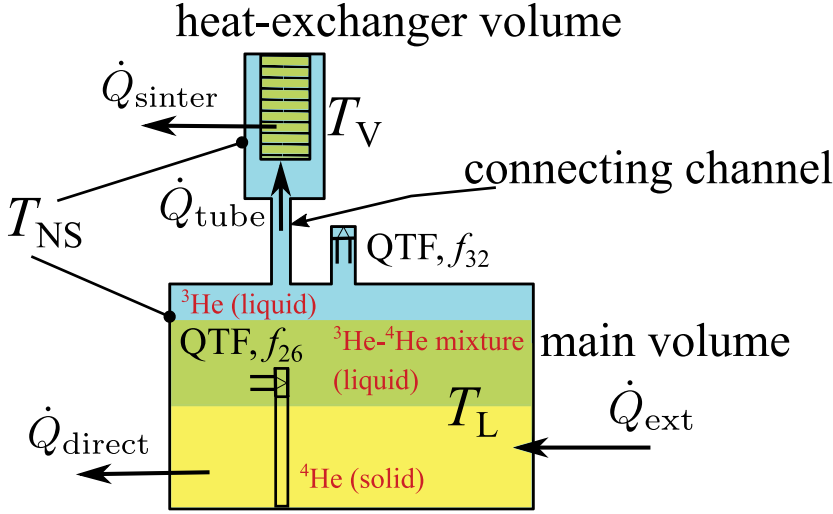


**Fig. 3.2** Simplified drawing of the experimental cell showing heat flows, temperatures and phases present during precool ( $T_{\text{NS}} < T_L, T_V$ ). Thermal gate is omitted here.

## 3.2 Computational model

The need behind modeling the experimental cell was the insensitivity of  $^3\text{He}$  QTF thermometer at the lowest temperatures. This dictated that we had to devise an alternate method to deduce the ultimate temperatures obtained in the melting runs. To get there, we had to analyze the heat flows and thermal connections present in our system. It was no trivial task because it was not possible to experimentally study each component independently.

A simplified view of the cell is shown in Fig. 3.2, where temperatures and heat flows are illustrated. The figure was drawn assuming that the nuclear stage is colder than helium in the cell, as is the case during precool. When the melt is carried out, the cell main volume becomes colder than the nuclear stage. During that time, the direction of the external heat leak  $\dot{Q}_{\text{ext}}$  stays the same, but the directions of the other three heat flows are reversed.

Our system has two significant thermal boundaries between liquid and metal, whose Kapitza resistance determines the flow of heat between the

cell and the nuclear stage: the plain wall of the main volume, and the sinter in the heat-exchanger volume. We assume that they obey a power law [69–71]

$$R_K = \frac{R_0}{AT^p}, \quad (3.11)$$

where  $A$  is the surface area ( $0.12 \text{ m}^2$  for wall, and  $10 \text{ m}^2$  for sinter), while  $R_0$  and  $p$  are constants that we still need to determine. In the following treatment though, we have combined  $R_0$  and  $A$  into one constant  $r = A/R_0$ . Hence, heat flow across a Kapitza bottleneck is

$$\dot{Q}_K(p, r, T) = \int_T^{T_{\text{NS}}} \frac{dT'}{R_K} = \frac{r}{p+1} (T_{\text{NS}}^{p+1} - T^{p+1}), \quad (3.12)$$

where  $r$  and  $p$  will assume different values for the sinter and the plain cell wall.

We begin with the main volume (L), from where the heat flows to the nuclear stage through two different paths: directly through the plain wall ( $\dot{Q}_{\text{direct}}$ ), and via the connecting channel ( $\dot{Q}_{\text{tube}}$ ) through the sinter in the heat-exchanger volume ( $\dot{Q}_{\text{sinter}}$ ).  $\dot{Q}_{\text{ext}}$  is the background heat leak, and additional heat to the system can also be brought by the flow-rate dependent losses  $\dot{Q}_f$  during crystal growth or melt. They can be due to nonideal superleak behavior, or the movement of the  $^3\text{He}$ –mixture phase boundary, for example. Finally, mixing (separating)  $^3\text{He}$  and  $^4\text{He}$  can absorb (release), heat according to Eqs. (3.6) or (3.9) ( $\dot{Q}_{\text{melt}}$ ). All in all, the total heat load of the main volume becomes

$$C_L \dot{T}_L(t) = \dot{Q}_{\text{melt}} + \dot{Q}_{\text{ext}} + \dot{Q}_f + \dot{Q}_{\text{direct}} + \dot{Q}_{\text{tube}}, \quad (3.13)$$

where  $T_L$  is the temperature of liquid in the main volume, and  $C_L = n_3^L C_3 + n_{m,3}^L C_{m,3}$  is its heat capacity with  $n_3^L$  and  $C_3$ , and  $n_{m,3}^L$  and  $C_{m,3}$  the amounts and heat capacities of  $^3\text{He}$  in the pure phase and mixture phase, respectively (cf. Eqs. (3.1) and (3.3)). In terms of Eq. (3.12), we get  $\dot{Q}_{\text{direct}} = \dot{Q}_K(p_L, r_L, T_L(t))$ .

Next, the heat load of the heat-exchanger volume (V) is

$$C_V \dot{T}_V(t) = \dot{Q}_{\text{sinter}} - \dot{Q}_{\text{tube}} + \dot{Q}_{\text{ext}V}, \quad (3.14)$$

where the first term is similar to the first term of Eq. (3.13) with  $C_V = n_3^V C_3 + n_{m,3}^V C_{m,3}$ , and  $T_V$  being the temperature of the liquid in the heat-exchanger volume, and  $\dot{Q}_{\text{sinter}} = \dot{Q}_K(p_V, r_V, T_V(t))$ .  $\dot{Q}_{\text{extV}}$  is the heat leak arriving directly to the heat-exchanger volume. We could not directly determine it, since that volume did not have its own thermometer. But, during the experiment we had no reason to suspect a large  $\dot{Q}_{\text{extV}}$  value. Furthermore, since the heat-exchanger volume had only one feedthrough (the normal capillary line which was blocked by solid  $^4\text{He}$  most of the time) while the main volume had three (superleak line and two QTF feedthroughs), we argue that it is reasonable to assume that heat leak to the main volume  $\dot{Q}_{\text{ext}}$  was large compared to  $\dot{Q}_{\text{extV}}$ . Hence, we have ignored  $\dot{Q}_{\text{extV}}$  from now on.

Due to the conservation of energy, all the heat that is not conducted through the plain cell wall must go through the  $^3\text{He}$ -filled connecting channel to the heat-exchanger volume. Since the channel was connected to the thermal gate, it was made of several sections with varying diameters but we will model it with a cylindrical channel with one effective diameter throughout, whose thermal resistance is

$$R_T = \frac{4l}{\kappa(T)\pi d^2}, \quad (3.15)$$

where  $\kappa(T)$  is the thermal conductivity of pure  $^3\text{He}$ , with  $l \approx 15\text{ cm}$  and  $d \approx 2.5\text{ mm}$  the effective length and diameter of the channel, respectively. Since we use a simplified model for the channel, at least 10% uncertainty in  $D = \frac{\pi d^2}{4l}$  is expected. The heat flow across such channel is given by

$$\dot{Q}_{\text{tube}} = \int_{T_V}^{T_L} \frac{dT'}{R_T} = D \int_{T_V}^{T_L} \kappa(T') dT'. \quad (3.16)$$

In normal fluid  $^3\text{He}$ , from the  $T_c$  up to our range of interest (about 10 mK), the thermal conductivity follows  $\kappa(T) = \kappa_0/T$  dependence, with the coefficient  $\kappa_0 = 9.69 \cdot 10^{-5} \frac{\text{W}}{\text{m}}$  interpolated from the data by Ref. [72]. But, below the  $T_c$  the behavior of  $\kappa(T)$  is not well established. We can proceed by dividing the integral into parts above and below the  $T_c$ . Then we can linearize the below  $T_c$  part, by assuming that the heat-exchanger volume

temperature  $T_V$  and the main volume temperature  $T_L$  are sufficiently close to each other. This gives

$$\begin{aligned}\dot{Q}_{\text{tube}} &= D \int_{\max(T_L(t), T_c)}^{\max(T_V(t), T_c)} \frac{\kappa_0}{T'} dT' + D \int_{\min(T_L(t), T_c)}^{\min(T_V(t), T_c)} \kappa(T') dT' \\ &= D\kappa_0 \ln \left[ \frac{\max(T_V(t), T_c)}{\max(T_L(t), T_c)} \right] + D\kappa_1(\bar{T}) [\min(T_V(t), T_c) - \min(T_L(t), T_c)],\end{aligned}\tag{3.17}$$

where  $\kappa_1$  is the superfluid  $^3\text{He}$  thermal conductivity evaluated at mean temperature of the integration bounds  $\bar{T}$ . We will utilize this split integral in our analysis in Section 4.3.

The total amount of  $^3\text{He}$  in the experiment was known, since it was introduced from room-temperature storage tanks with determined contents. It ranged from 700 to 1000 mmol during the experiment, of which 170–400 mmol was in the lower bellows volume to ensure there was saturated mixture there. The rest 460–700 mmol was in the melting cell, with 190 mmol in the heat-exchanger volume and the connecting channel. The heat-exchanger volume is almost completely filled with pure liquid  $^3\text{He}$ , but we have assumed some mixture to be trapped in the porous sinter material. We had 11 g of sinter with density  $10.5 \text{ g/cm}^3$  and filling factor 0.5 giving  $2 \text{ cm}^3$  of free volume within it. Filling it would take 90 mmol of saturated mixture, of which about 7 mmol is  $^3\text{He}$ . The  $^3\text{He}$  that was left after all that was in the main volume of the cell. The amount of solid and mixture was calculated based on the known total volume of the cell ( $82 \text{ cm}^3$ ), the measured amount of  $^4\text{He}$  added (removed) to grow (melt) the solid phase, Eq. (3.10), and the known molar volumes of the phases.

To enable us to utilize this thermal model to calculate the lowest temperatures, we first need to determine the unknown parameters for our system. This includes the Kapitza coefficients for the sinter and the plain cell wall ( $r_V$ ,  $p_V$  and  $r_L$ ,  $p_L$ ), external heat leak ( $\dot{Q}_{\text{ext}}$ ), flow-rate dependent heat leak ( $\dot{Q}_f$ ), as well as the thermal conductivity of superfluid  $^3\text{He}$  in the connecting channel ( $\kappa_1$ ). Additionally, we always need to know the quantities of various helium phases present at each moment. A large portion of Chapter 4 is spent on tackling these issues.

But before that, now that we have discussed about the functional form of Kapitza resistance, let us first put the cooling powers obtainable with the melting process into perspective. We had 100 pW at 100  $\mu\text{K}$ , and let us

assume we want to achieve the same with an external cooling that needs to overcome the Kapitza bottleneck. We use Eq. (3.11), with  $p = 2$ , and  $R_0 = 7 - 30 \text{ m}^2\text{K}^3/\text{W}$  [28, 69] for the Kapitza coefficients between mixture and metallic sinter. If we assume that the coolant is at zero-temperature, the cooling power is given by  $|\int_0^T \frac{dT'}{R_K}| = \frac{A}{3R_0} T^3$ , from which we can solve that the area needed is  $A = 2000 - 9000 \text{ m}^2$ . Such areas are plausible, yet not easy, to achieve in practice. At even lower temperatures, the situation becomes rapidly more challenging: for example 100 pW at 60  $\mu\text{K}$  would require about 25 000  $\text{m}^2$  surface area. Using the melting method, the same cooling power can be achieved with about 300  $\mu\text{mol/s}$   $^3\text{He}$  phase-transfer rate. Adding more and more sinter would bring further complications due to the relaxation of  $^3\text{He}$  concentration in the pores of the sinter introducing a time-dependent heat load [69].

## Chapter 4

### Results

Here we will review the key findings of our experiment. We begin in Section 4.1 by discussing the behavior of the quartz tuning forks at low temperatures, focusing on the pure  $^3\text{He}$  QTF and its utilization as a thermometer. Next, we determine the remaining unknown parameters in our computational model in Sections 4.2–4.4 before moving on to analyze the melting data. We first study runs closer to the  $T_c$  in Section 4.5 to confirm the validity of our model, where we also take a look at the performance of the thermal gate, and the bellows-operated melting. Then we estimate the ultimate temperatures achieved in the melting experiment in Section 4.6, and study how altering certain parameters would have affected the lowest possible temperature.

To set up the upcoming discussion, Fig. 4.1 shows an example of a successful melting run. We have converted the measured pure  $^3\text{He}$  QTF width to temperature with the calibration to be discussed in Section 4.1. The graph begins at the moment when the final crystal growth period ended. As the precool goes on, temperature typically saturates somewhere slightly below  $500\ \mu\text{K}$ . Then, solid is melted bringing the temperature down until we reach the saturation in the QTF response, after which it slowly relaxes back towards the initial temperature during the warm-up period. The equilibrium temperatures before and after melting were not necessarily the same. The figure also illustrates how sensitive the precool relaxation is to the amount of mixture, when we compare the measured behavior to computed behaviors at various mixture amounts. The relaxation is dependent on the total heat capacity of the system, and as we saw in Section 3.1, at these temperatures the mixture is its main contributor.

We can determine the amount of solid  $^4\text{He}$  in the cell in two ways: from the amount of transferred  $^4\text{He}$  through the superleak and Eq. (3.10), or

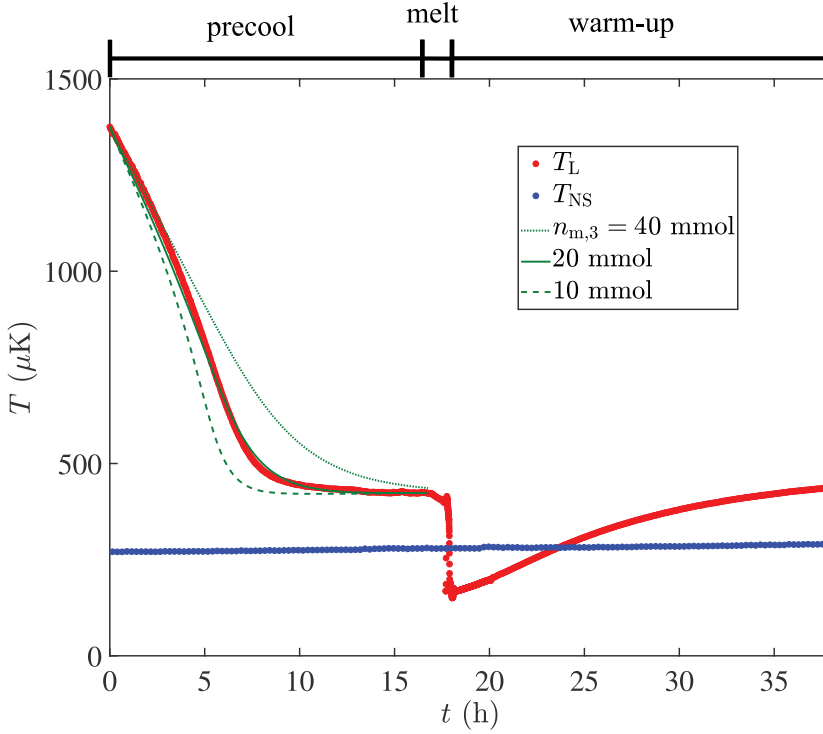


**Fig. 4.1** Example of data obtained during a successful melting run, with different stages labeled. The measured nuclear stage temperature  $T_{\text{NS}}$  is shown in blue, while the measured cell main volume temperature  $T_{\text{L}}$  is shown in red. The green lines are computed  $T_{\text{L}}$  with different amounts of  $^3\text{He}$  in the mixture phase (shown in the legend).

by examining the relaxation time towards the nuclear stage temperature. The relaxation time fixes the mixture amount, and since the total amount of  $^3\text{He}$  was known, we can calculate the amount of solid. We found that these two ways were always in agreement within 10%.

## 4.1 Quartz tuning forks at low temperatures

Figure 4.2 illustrates the behavior of both the pure  $^3\text{He}$  and the mixture QTF during our experiment. The mixture phase does not undergo any phase transitions under 2 K, below which  $^4\text{He}$  component is superfluid

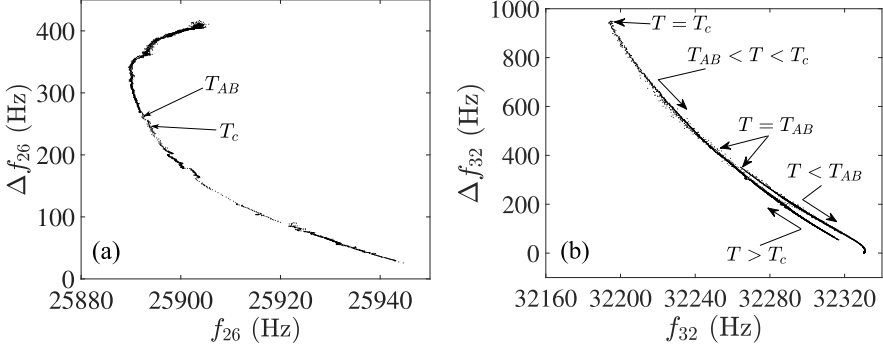


**Fig. 4.2** Resonance width against resonance frequency for both  $^3\text{He}$ – $^4\text{He}$  mixture QTF  $f_{26}$  (a), and  $^3\text{He}$  QTF  $f_{32}$  (b). Significant points of temperature are also shown.

but  $^3\text{He}$  is in the normal state. Thus its width increases with decreasing temperature, until eventually saturating to about 405 Hz below 1 mK (Fig. 4.2a). The frequency, on the other hand, exhibits a minimum at around 25890 Hz, whose position depends on the geometry of the experimental cell [50, 73], as it is caused by the quasiparticle scattering from the walls of the experimental volume. The early saturation meant that this QTF was not very useful as a thermometer. Had the  $^3\text{He}$  component become superfluid at the ultra-low temperatures, the width would have started to decrease rapidly from the saturation value.

In Fig. 4.2b, the measured pure  $^3\text{He}$  QTF width initially increases with decreasing temperature, as did the mixture QTF. But below the  $T_c$  (at 926 Hz width), the width rapidly starts to fall as the number of  $^3\text{He}$  quasiparticles decreases reducing energy loss from the oscillator. Then at about  $0.92T_c$ ,  $^3\text{He}$  goes from A-phase to B-phase which is observed as a sudden jump in the width from about 424 to 350 Hz. As the temperature decreases more, we eventually reach the ballistic regime at about 20 Hz width, after which the resonance frequency no longer changes in proportion with the width.

In Fig. 4.3, we take a closer look at this ballistic cross-over, as well as compare it to an independent measurement [IV] performed by the ROTA-group of our laboratory in their nafen-filled experimental cell [74, 75]. Nafen is a nematically ordered aerogel, whose strands are oriented along the same direction. We note that below the ballistic cross-over the fre-

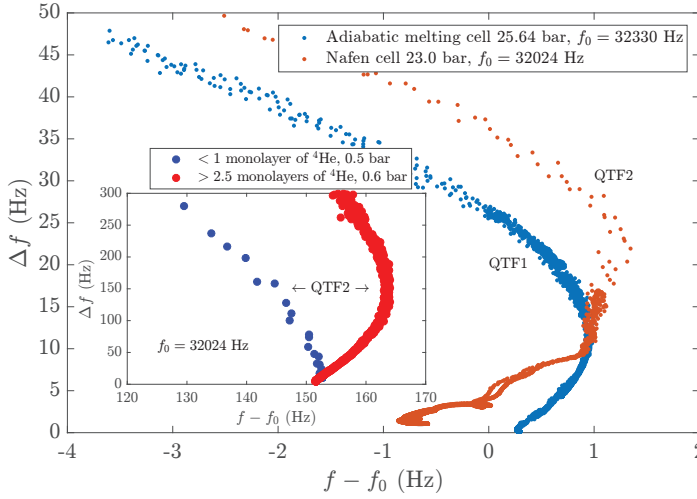


**Fig. 4.3** QTF resonance width as a function of resonance frequency in the melting experiment (QTF1) compared to an independent measurement done by the ROTA-group (QTF2). Inset shows the QTF2 behavior with small  $^4\text{He}$  amounts in the system at low pressures.

quency response reverses; it starts to slowly decrease with temperature, instead. This reversing behaviors seems to be dependent on whether there is enough  $^4\text{He}$  present in the system. The inset of Fig. 4.3 shows that if there is less than 1 monolayer of  $^4\text{He}$  present on the surfaces of the system, the frequency merely saturates at sufficiently low temperature. Only when the  $^4\text{He}$  coverage is increased to above 2.5 monolayers the maximum in the frequency occurs. In our melting cell, even if we call our thermometer resonator " $^3\text{He}$  QTF", it is not in ideal bulk  $^3\text{He}$ . Since there is a lot of  $^4\text{He}$  available in the system, all surfaces are maximally covered by it due to superfluid film flow. This, of course, includes the surfaces of the quartz oscillators.

The presence of a  $^4\text{He}$  layer on the QTF surface can alter the  $^3\text{He}$  quasi-particle scattering conditions [76–80], which can also depend on the thickness of the film. However, a theoretical description of the phenomenon is not yet well established. It is not unequivocally clear that the maximum in the frequency occurs exactly at the ballistic cross-over point. But, since at these ultra-low temperatures, it is the only notable reproducible feature in

the fork response, it can be used as a reference point when constructing a QTF temperature calibration.

#### 4.1.1 Calibration

In normal fluid  $^3\text{He}$ , we can use the hydrodynamical model of Ref. [44] with the bulk  $^3\text{He}$  viscosity from Ref. [48] to convert the measured resonance width into temperature

$$\left(\frac{T}{\text{mK}}\right)^2 = \frac{1}{6.65} \left\{ \left[ \left( \frac{\Delta f_{32}}{\mathcal{A}} \right)^2 \left( \frac{f_{\text{vac}}}{f_{32}} \right)^4 \frac{4\pi}{\rho f_{32}} \frac{\text{kg Hz}}{\text{m}^3} - 10^{-5} \right]^{-1} - 12.8 \right\}, \quad (4.1)$$

where  $f_{32}$  and  $\Delta f_{32}$  are the measured resonance frequency and width, respectively,  $f_{\text{vac}} = 32765.9\text{Hz}$  is the vacuum resonance frequency,  $\rho = 112.7\text{g/cm}^3$  is the density of liquid  $^3\text{He}$ , while  $\mathcal{A} = 0.429\text{Hz}$  is the fitting parameter determined from the  $T_c$  values of the resonance frequency and width, 32187 Hz and 926 Hz, respectively.

For the superfluid phase we constructed a phenomenological model using  $T_c$  and  $T_{AB}$  as fixed points. Since those two are at relatively high temperature, and close to each other, we additionally used the location of the ballistic-crossover resonance-frequency maximum as our third semi-free calibration point with temperature fixed to  $0.25T_c$ , but the corresponding width was allowed to vary between 10–30 Hz while setting up the calibration. We ended up with

$$\frac{T}{T_c} = \left[ 1 + \frac{\Delta f_{32}^{0.3} - (\Delta f_b - \Delta f_0)^{0.3}}{\mathcal{B}^{0.3}} - \frac{\Delta f_{32}^{1.4} - (\Delta f_b - \Delta f_0)^{1.4}}{\mathcal{C}^{1.4}} \right] \left[ 4 - \mathcal{D} \ln \left( \frac{\Delta f_{32} - \Delta f_0}{\Delta f_b - \Delta f_0} \right) \right]^{-1} \quad (4.2)$$

for  $^3\text{He-B}$ , and

$$\frac{T}{T_c} = \left[ 1 - \mathcal{E} \exp \left( -\frac{\Delta f - \Delta f_{AB}}{\mathcal{F}} \right) \right] \quad (4.3)$$

for  $^3\text{He-A}$ , where  $\Delta f_b = 22\text{Hz}$  is the chosen width for the ballistic crossover,  $\Delta f_0 = 0.14\text{Hz}$  the residual width,  $\Delta f_{AB} = 424\text{Hz}$  the width at the AB-transition, and  $\mathcal{B} = 2.138\text{ kHz}$ ,  $\mathcal{C} = 391.0\text{ Hz}$ ,  $\mathcal{D} = 1.250$ ,  $\mathcal{E} = 0.085$ , and  $\mathcal{F} = 129.5\text{ Hz}$  are the fitting parameters. We required that the formula exhibited monotonous dependence between width and temperature

with smooth derivative across the entire temperature range. Furthermore, temperature and its derivative had to be continuous at the  $T_c$  and the  $T_{AB}$ . The exponents 0.3 and 1.4 in Eq. (4.2) were determined empirically to produce credible behavior across the whole span of  ${}^3\text{He-B}$ .

#### 4.1.2 Saturation in the response

Next, in Fig. 4.4, we take a look at the QTF response during the coldest stages of a melting (cf. Fig. 4.1). Initially, the width drops with temperature as expected, but below 180 mHz the monotonous response is broken and there appear resonance-like anomalies that form kinks and loops in the frequency–width graph. The width does not go below 150 mHz, while the frequency decreases by about 30 mHz during the melt. The intrinsic damping of the QTF was expected to cause residual width of order 10 mHz, but the observed response saturates at a more than 10 times higher value. Similar behavior was also seen in the experiment by ROTA, but only at pressures below the  ${}^4\text{He}$  crystallization pressure. Thus, it seems that the liquid  ${}^4\text{He}$  layer on the QTF is responsible for the additional damping.

The resonance-like features in Fig. 4.4 can be caused by the approaching mixture–pure  ${}^3\text{He}$  phase boundary. At the beginning of the melt, the experimental cell is mostly filled by solid  ${}^4\text{He}$  and pure  ${}^3\text{He}$  with a small amount of remnant mixture. As the solid is melted, the amount of the

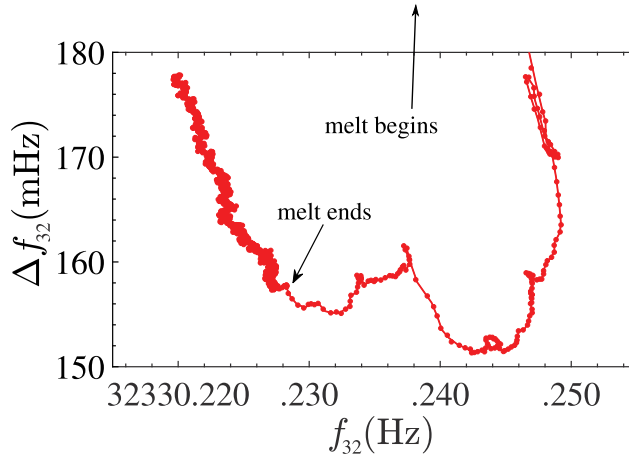


**Fig. 4.4** QTF resonance width as a function of resonance frequency during and after the melting process. Melting begins outside the frame at about  $\Delta f_{32} = 8$  Hz.

mixture phase increases, while the solid phase and the  $^3\text{He}$  phase are reduced. As the mixture phase containing  $^4\text{He}$  approaches the QTF, it can increase the thickness of the  $^4\text{He}$  film covering the QTF due to superfluid film flow. This effectively increases the mass of the oscillator, which could cause the observed  $\sim 30$  mHz shift in the resonance frequency, and possibly also cause specific features at certain mixture amounts (*i.e.* at certain crystal sizes). For example, the width backtrack immediately below 32330.240 Hz was somewhat reproducible during other melts as well. However, the measured frequency varied of order 100 mHz between different melts.

Since below about 0.2 Hz width there appear anomalous features in the QTF response, we must conclude that the  $^3\text{He}$  QTF is no longer a reliable thermometer of bulk liquid below that width. This is why we now focus on completing the computational model to enable us to evaluate the temperatures even when the QTF was no longer reliable.

## 4.2 Kapitza resistances

The challenge in determining the three most significant thermal contact parameters, the Kapitza resistances of the plain cell wall and the sinter, and the thermal conductivity of the connecting channel, is that they could not be analyzed independently. Especially, the thermal properties of sinter and the connecting channel were intertwined. Fortunately, certain stages of the experimental cycle were more sensitive to one than the others. At the early stage of precool (near 10 mK), the cooling rate is heavily influenced by the properties of the plain cell wall, as then a significant amount of heat still flows through it, while the heat flow through the channel is limited by the poor conductivity of normal fluid  $^3\text{He}$ . But, below the  $T_c$ , the importance of the plain cell wall rapidly falls off, because it has relatively small surface area compared to the sinter. The crossing of the  $T_c$ , on the other hand, is sensitive to the thermal conductivity of  $^3\text{He}$  in the connecting channel, as at the  $T_c$  it momentarily increases notably due to the normal fluid–superfluid counterflow effect. Below that, the Kapitza bottleneck of the sinter in the heat-exchanger volume will become more and more important to the overall behavior of the system.

Hence, the plain cell wall Kapitza resistance can be determined quite independently, as we will see in Section 4.2.1, but the assumed properties of sinter and the connecting channel were varied together during the analysis, and the values presented here are a result of a sequence of recursive fitting procedures.

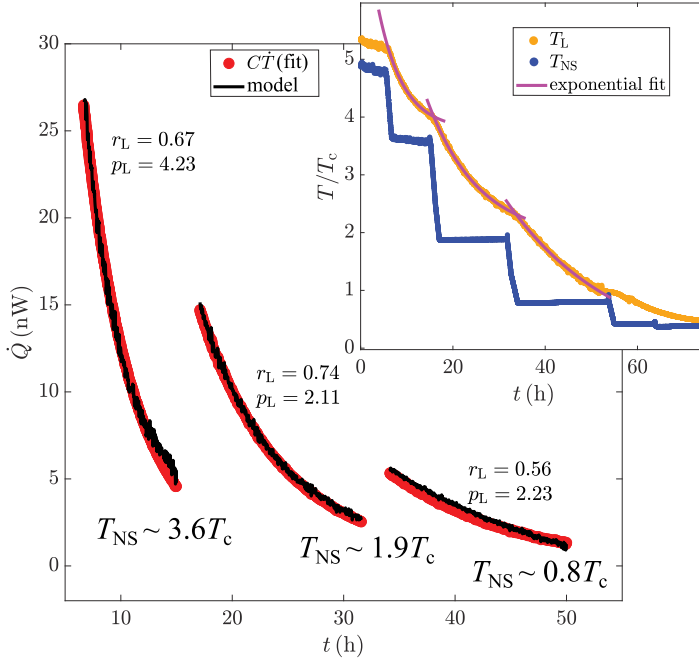


**Fig. 4.5** Heat transferred between the main volume of the cell and the nuclear stage directly through the plain cell wall at various temperatures. Inset shows the measured cell main volume temperature  $T_L$  and the nuclear stage temperature  $T_{NS}$ , as well as exponential fits to the  $T_L$  data at each cooling step.

### 4.2.1 Plain cell wall

When considering the early stages of precool, we can simplify the cell main volume heat balance equation Eq. (3.13) to

$$C_L \dot{T}_L = \frac{r_L}{p_L + 1} (T_{NS}^{p_L+1} - T_L^{p_L+1}) + D\kappa_0 \ln\left(\frac{T_{NS}}{T_L}\right), \quad (4.4)$$

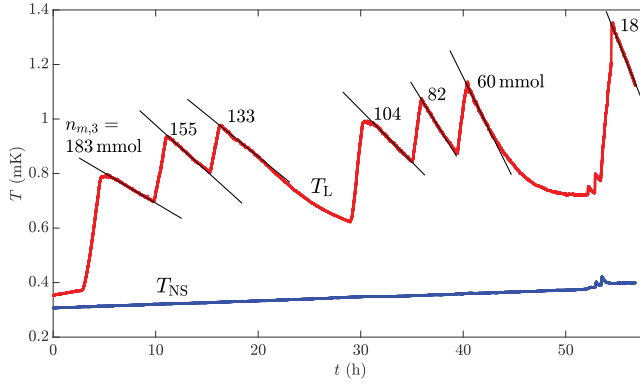
since we can assume that the heat-exchanger volume is at the same temperature as the nuclear stage,  $^3\text{He}$  is in normal state everywhere, and  $\dot{Q}_{\text{melt}} = \dot{Q}_f = 0$ , because the amount of solid is not changing. The heat flow through the wall is of order 10 nW at these temperatures, meaning that we can ignore the external heat leak  $\dot{Q}_{\text{ext}}$  of order 0.1 nW.

Figure 4.5 shows a run where we decreased the nuclear stage temperature stepwise, and observed the relaxation of temperature in the cell. To have smoother derivative  $\dot{T}_L$ , we fitted exponential functions to the measured temperature data at each cooling step (inset of Fig. 4.5). Since the normal fluid  $^3\text{He}$  thermal conductivity  $\kappa_0$  in the connecting channel is known based on interpolation of Ref. [72] data, we are left with  $p_L$  and  $r_L$  to be fitted in Eq. (4.4).

Comparison between the smoothed  $C_L \dot{T}_L$  data and the computation performed with the chosen Kapitza parameter values are shown in the main panel of Fig. 4.5, where the model lines were calculated using the original measured  $T_L$  data. Since  $T_L$  and  $T_{NS}$  differ more than credible at the start of the precool, due to PLM-thermometer or QTF calibration, or both, being slightly off at higher temperatures, the parameters fitted to the first temperature step obviously overestimate the Kapitza parameters. On the other hand, if we increase  $T_{NS}$  by 5% uniformly throughout the temperature range, the reevaluated fit likely underestimates the parameters instead. After analyzing 5 more similar datasets to that of Fig. 4.5, we ended up with  $p_L = (2.6 \pm 0.2)$  and  $r_L = (0.7 \pm 0.2) \text{WK}^{-p_L-1}$ , which are average values across all 5 datasets with adjusted/unadjusted  $T_{NS}$  temperatures. The confidence bounds were determined as the standard error of the fitted parameter values. Since the estimated cell wall area was  $0.12 \text{ m}^2$ , we get value  $R_{0,L} = (0.17 \pm 0.05) \text{ m}^2 \text{ K}^{p_L+1} \text{ W}^{-1}$ , for the area scaled constant  $R_0 = A/r$  of Eq. (3.11).

### 4.2.2 Sinter

The Kapitza parameters of the sinter in the heat-exchanger volume were determined by periodically altering the amount of solid  $^4\text{He}$  at around 1 mK, and recording the following relaxation towards the nuclear stage temperature. Example of such data is shown in Fig. 4.6. Changing the crystal size alters the amount of mixture in the system, and thus the total heat capacity. At these temperatures, mixture already is the main contributor to the total heat capacity. We can no longer assume that the heat-exchanger volume is at the same temperature as the nuclear stage  $T_V \neq T_{NS}$ . Furthermore, we cannot ignore the external heat leak  $\dot{Q}_{\text{ext}}$  anymore, and the limited conductivity of the connecting channel also plays a role. Thus, the fitting procedure involved simulating the entire system using Eqs. (3.13) and (3.14), and the superfluid  $^3\text{He}$  thermal conductivity which will be discussed in Section 4.3, while altering the sinter Kapitza parameters  $p_V$  and  $r_V$ .



**Fig. 4.6** Nuclear stage temperature  $T_{\text{NS}}$  and cell main volume temperature  $T_{\text{L}}$  while growing solid  $^4\text{He}$  stepwise. The amount of  $^3\text{He}$  in the mixture phase after each step is shown next to the  $T_{\text{L}}$  graph. The black lines are linear fits to the data with slopes  $-6.2 \cdot 10^{-6}$ ,  $-9.5 \cdot 10^{-6}$ ,  $-8.5 \cdot 10^{-6}$ ,  $-1.1 \cdot 10^{-5}$ ,  $-1.7 \cdot 10^{-5}$ ,  $-2.1 \cdot 10^{-5}$ , and  $-2.6 \cdot 10^{-5}$  mK/s from left to right.

Using the linear fits of Fig. 4.6, we first determine the time it takes the main volume to cool across a certain temperature interval, and then in Fig. 4.7 we attempted to reproduce the behavior using the computational model. In Fig. 4.7a, we always kept  $\dot{Q}_{\text{ext}}$  constant and varied  $p_{\text{V}}$  while keeping  $r_{\text{V}}$  constant in the computation, or vice versa. The computation is more sensitive to the exponent  $p_{\text{V}}$  than the coefficient  $r_{\text{V}}$ , giving us a good idea for the appropriate exponent value. Then, in Fig. 4.7b the constant  $\dot{Q}_{\text{ext}}$  is maintained, but this time we adjusted  $r_{\text{V}}$  for each exponent  $p_{\text{V}} = 1.6 - 1.8$ , with restriction that at 10 mK each combination would give equal resistance value. That restriction ensured consistent model behavior above the  $T_{\text{c}}$ . Now,  $p_{\text{V}} = 1.7$ , and  $r_{\text{V}} = 0.20 \text{ WK}^{-p_{\text{V}}-1}$  seemed the most appropriate. Yet, as we vary the external heat leak in Fig. 4.7c, we note that similar spread in the computed relaxation time is observed as in Fig. 4.7b, giving us an estimate of the confidence bounds of the fitted parameters.

Next, Fig. 4.8 shows similar measurement done over other temperature intervals with different total  $^3\text{He}$  amounts, where Fig. 4.8a was obtained during a stepwise melt, and Fig. 4.8b during a stepwise growth. The fits were done in similar fashion to Fig. 4.7b. The computations in the Fig. 4.8a would favor exponent 1.6, but there the temperature was already so low that the QTF measurement was likely hampered by the saturation behavior. In Fig. 4.8b either 1.8 or 1.7 works with 1.6 being already slightly too low. Thus we conclude that the satisfactory sinter Kapitza pa-

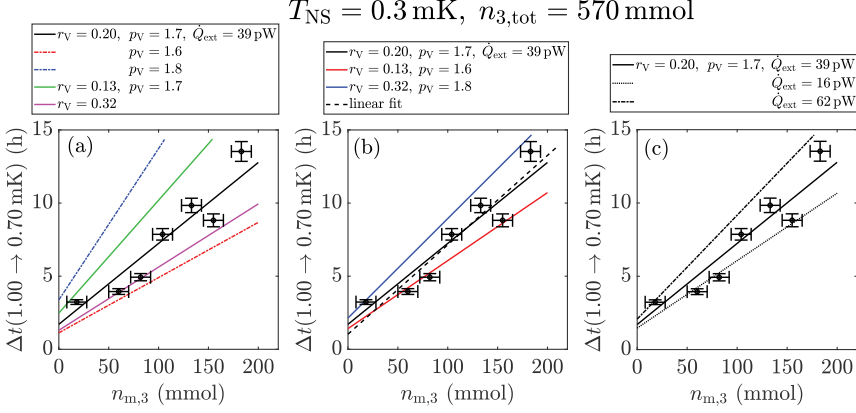


**Fig. 4.7** Relaxation of the cell main volume temperature from  $T_L = 1.00 \text{ mK}$  to  $0.70 \text{ mK}$  as a function of  $^3\text{He}$  amount in the mixture phase (datapoints). The lines were obtained by simulating the system with various sinter Kapitza parameter values: (a) constant  $r_V$ /changing  $p_V$ , and changing  $r_V$ /constant  $p_V$ , with a constant external heat leak  $\dot{Q}_{\text{ext}}$ , (b) adjusted  $r_V$  for each exponent with a constant heat leak (dashed line shows a linear fit to the datapoints, for comparison), and (c) constant  $r_V$  and  $p_V$  at various heat leaks.

rameters, with uncertainties taken into account, would be  $p_V = (1.7 \pm 0.1)$  and  $r_V = (0.2 \pm 0.1) \text{ WK}^{-p_V-1}$ . The area scaled constant becomes  $R_{0,V} = (50 \pm 30) \text{ m}^2 \text{ K}^{p_V+1} \text{ W}^{-1}$ , as sinter had  $10 \text{ m}^2$  surface area.

We should note that the parameters determined around  $1 \text{ mK}$  may not remain constant throughout the entire temperature range of the experiment. This is illustrated in Fig. 4.9, where we take a look at the time the main volume required to cool from the  $T_c$  to the  $T_{AB}$ , at different total  $^3\text{He}$  amounts. Near the  $T_c$  with large crystal sizes, superfluid  $^3\text{He}$  is the dominant contribution to the total heat capacity of the system. Each datapoint in Fig. 4.9 represents average  $T_c \rightarrow T_{AB}$  time taken over multiple precoolings with the certain amount of  $^3\text{He}$ . We compare them against values calculated by assuming constant nuclear stage temperature  $T_{\text{NS}} = 0.5 \text{ mK}$ , with the external heat leak  $\dot{Q}_{\text{ext}}$  being negligible at these temperatures. We chose to have fixed sinter Kapitza exponent value  $p_V = 1.7$ , which meant that to have the best fit to this particular dataset, we had to decrease the coefficient from  $r_V = 0.20 \text{ WK}^{-p_V-1}$  to  $r_V = 0.15 \text{ WK}^{-p_V-1}$ . Nevertheless, this adjusted value is still within our confidence intervals. Since the constant  $r_V$  works well at temperatures below  $1 \text{ mK}$ , where our main interest lies, we chose not to include any temperature dependence for it in our com-

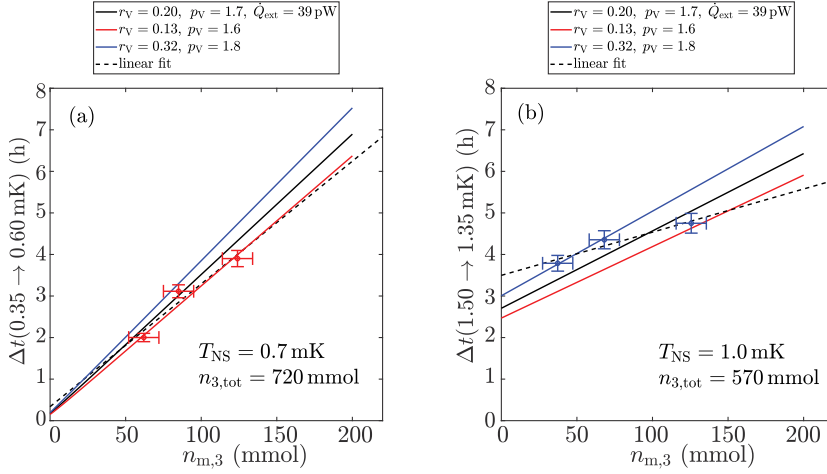


**Fig. 4.8** Relaxation of the cell main volume temperature from  $T_L = 0.35$  mK to  $0.60$  mK after melting solid periodically (a), and from  $T_L = 1.50$  mK to  $1.35$  mK after growing solid periodically (b) at different mixture amounts (datapoints). Solid lines were obtained by simulating the system with different Kapitza resistance parameters (cf. Fig. 4.7b), while the dashed lines are linear fits to the datapoints, for comparison.

putational model. Rather we mainly used  $r_V = 0.20 \text{ WK}^{-p_V-1}$  at all our low temperature calculations with an option to use a slightly smaller value when analyzing data near the  $T_c$ .

To enable comparison with the measurements made by others, we can round our determined sinter Kapitza exponent to the nearest integer (2), and scale the coefficient  $R_0$  to match it by utilizing the 10 mK restriction mentioned before ( $12 \text{ m}^2 \text{K}^3 \text{W}^{-1}$ ). Ref. [28] observed that the Kapitza resistance between their sinter and saturated  $^3\text{He}$ – $^4\text{He}$  mixture at 10 bar followed the exponent  $p = 2$  with the coefficient  $R_0$  between  $10$ – $30 \text{ m}^2 \text{K}^3 \text{W}^{-1}$  depending on the magnitude of the magnetic field in their experiment. Ref. [69], on the other hand, measured the Kapitza resistance of the saturated mixture and sinter, where the phase-separation boundary was partly in the sinter, receiving either  $p = 2$  or  $p = 3$  with the coefficients  $R_0$   $6.5 \text{ m}^2 \text{K}^3 \text{W}^{-1}$  and  $0.0029 \text{ m}^2 \text{K}^4 \text{W}^{-1}$ , respectively. For pure  $^3\text{He}$ –B they could make exponents 1, 2 or 3 work with coefficients about  $700 \text{ m}^2 \text{K}^2 \text{W}^{-1}$ ,  $0.5 \text{ m}^2 \text{K}^3 \text{W}^{-1}$  and  $0.2 \cdot 10^{-3} \text{ m}^2 \text{K}^4 \text{W}^{-1}$ , respectively. The comparison is also shown in Table 4.1.

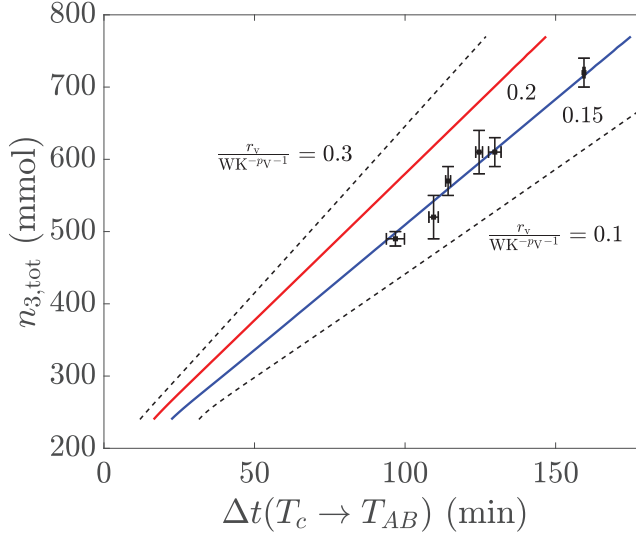


**Fig. 4.9** Time it took for the cell main volume to cool from the  $T_c$  to the  $T_{AB}$  versus the total amount of  $^3\text{He}$  in the experimental cell. Various lines are computed  $T_c \rightarrow T_{AB}$  times, assuming no  $^3\text{He}$  in the mixture phase. The dashed black lines show the behavior at the upper and lower end of the  $r_V$  confidence bounds, while the red line is the low temperature fit, and blue the best  $r_V$  to the current dataset.

Our sinter Kapitza parameters are in line with the mixture parameter values determined by others, even if the bulk of the heat-exchanger volume is filled by pure  $^3\text{He}$ . Since superfluid  $^4\text{He}$  is readily available in our system, all available surfaces are covered by it and sinter has a lot of surface area. That was why earlier we made the assumption that the sinter was filled with saturated mixture, and the Kapitza parameter comparison seems to agree with it. It is not certain that the mixture in the sinter is precisely at the bulk saturation concentration  $x_3 = 8.1\%$ , but we deemed it a reasonable approximation.

### 4.3 Superfluid $^3\text{He}$ thermal conductivity

In superfluid, the total thermal conductivity is a sum of diffusive and hydrodynamic parts [82–86]. The diffusive part is similar to any ordinary fluid, for it is a result of the interactions between the (quasi)particles. But the hydrodynamic portion is specific to superfluid systems as it is caused

This work		(mix)[28]		(mix)[69]		$^3\text{He-B}$ [69]		$^3\text{He-B}$ [81]	
$p$	$R_0$	$p$	$R_0$	$p$	$R_0$	$p$	$R_0$	$p$	$R_0$
1.6	80	2	20	2	6.5	1	700	1	1100
1.7	50			3	0.0029	2	0.5		
1.8	20					3	$0.2 \cdot 10^{-3}$		
(2)	(12)								

**Table 4.1** Comparison between our sinter Kapitza parameters and the values received by others in saturated mixture and  $^3\text{He-B}$ . The unit of  $R_0$  is  $\text{m}^2\text{K}^{p+1}\text{W}^{-1}$ . The values in parentheses are our determined Kapitza exponent rounded to the closest integer, and correspondingly scaled  $R_0$  (see text), to enable comparison.

by normal fluid–superfluid counterflow effect, where superfluid component flows towards warm parts, and to maintain uniform fluid density, normal fluid component must flow the opposite way. This phenomenon is especially important at temperatures near the  $T_c$ . Far below it, where there is practically no normal component anymore, the diffusive conductivity takes over again. Our measurement gave information on the total conductivity.

When we know the Kapitza resistance parameters, we can solve Eqs. (3.13) and (3.14) for the heat-exchanger volume temperature  $T_V$ , which is needed to resolve the thermal conductivity of  $^3\text{He}$  in the channel connecting the heat-exchanger to the main volume. Had there been a thermometer QTF also in the heat-exchanger volume, we could have determined the conductivity independently, but since that was not the case we had to study it in conjunction with the Kapitza parameters.

As we have the temperature at each end of the channel, and heat flows through the other routes, we get the heat flow across the channel and can solve Eq. (3.17) for the unknown superfluid  $^3\text{He}$  thermal conductivity  $\kappa_1$  as a function of the channel temperature  $\bar{T}$ .

Figure 4.10 shows the averaged result of our analysis that involved 8 cooldowns from 3 mK to 0.5 mK performed by demagnetization of the nuclear stage, and 9 cooldowns from 1.5 mK to 0.5 mK after growing solid  $^4\text{He}$  below the  $T_c$ . To access temperatures below 0.5 mK, we also analyzed 5 post-melting warm-up periods with the low-temperature limit determined by the saturation of the main volume QTF thermometer. We averaged the measured QTF data over 7–20 min intervals, depending on the scatter on the data, to reduce the noise in its time derivative  $\dot{T}_L$ . The confidence bounds in Fig. 4.10 involve the uncertainties in the Kapitza parameters discussed in Section 4.2, and 10% variation in the channel di-

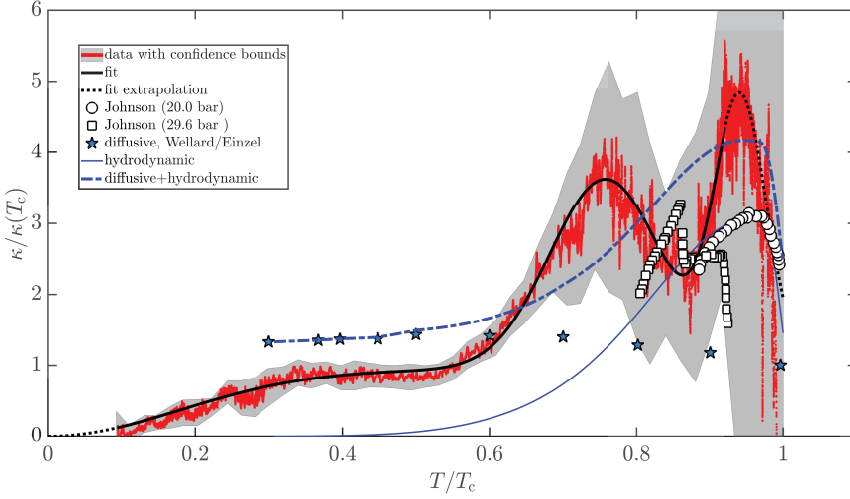


**Fig. 4.10** Thermal conductivity of superfluid  $^3\text{He}$  as a function of temperature relative to the superfluid transition temperature  $T_c$  is shown in red with the shaded gray area representing the confidence bounds. Thermal conductivity values are scaled by the normal fluid value at the  $T_c$  ( $0.037 \frac{\text{W}}{\text{Km}}$  [72]). The solid black line is a multi-Gaussian fit to the data, and the dotted black lines show the extrapolation of the fit at  $T < 0.1T_c$  and at  $T > 0.92T_c$ . Thermal conductivity data by Johnson *et al.* [87] at 20.0 bar ( $\circ$ ) and at 29.6 bar ( $\square$ ), alongside with diffusive thermal conductivity ( $\star$ ) by Wellard *et al.* [88] (further analyzed by Einzel [85]), as well as hydrodynamic conductivity (solid blue line) calculated from Eq. (4.5) are shown for comparison. The dash-dotted blue line shows the diffusive and hydrodynamic conductivities combined.

mension parameter  $D$ . Furthermore, we had allowed the external heat leak  $\dot{Q}_{\text{ext}}$  to vary between 20 and 80 pW across the fits. We fitted a function of form  $\kappa/\kappa(T_c) = g_1(T) + (\mathcal{K}_2 - g_2(T)) + g_3(T)$  to the data, where  $g_i = \mathcal{K}_i \exp\left[-\left((T - T_{0,i})/\sigma_i\right)^2\right]$  is a Gaussian function with parameters  $\mathcal{K}_i$ ,  $T_{0,i}$  and  $\sigma_i$  listed in Table 4.2. The relation is completely phenomenological; we wanted to end up with a smooth function to be inserted to the computational model.

Near the  $T_c$  our analysis procedure does not yield accurate results, which is caused by two things. First, as we cool through the  $T_c$   $^3\text{He}$  undercools, *i.e.*, temperature of liquid is already below the  $T_c$  but it is still in normal state, and secondly, the QTF calibration formula changes at the  $T_c$  from normal fluid viscosity dependent calibration to our phenomenological

$i$	$\mathcal{K}_i/\kappa(T_c)$	$T_{0,i}/T_c$	$\sigma_i/T_c$
1	2.68	0.76	0.11
2	0.94	0	0.25
3	3.76	0.94	0.05

**Table 4.2** List of the parameters used in the multi-Gaussian fit of Fig. 4.10

one (cf. Section 4.1.1). In combination these two cause a small artificial jump in the temperature determined from the QTF width at the  $T_c$  causing a large apparent derivative. As a further complication, just below the  $T_c$  we can have a situation where the superfluid  $^3\text{He}$  in the heat-exchanger volume is already in the B-phase, while the main volume is still in the A-phase, and the AB phase-boundary can be somewhere in the connecting channel causing irregular behavior in the determined thermal conductivity [89]. Thus, we conclude that we can gain reasonable thermal conductivity data only in  $^3\text{He}$ -B superfluid ( $T < 0.92T_c$ ). A suggested extrapolation to the A-phase is also shown in Fig. 4.10.

As we go deeper in the B-phase, the conductivity first decreases to a local minimum at  $0.85T_c$ , below which we find a local maximum at  $0.75T_c$  followed by a plateau between  $0.5T_c$  and  $0.3T_c$ . As we approach the zero-temperature limit, conductivity then monotonously falls off.

Figure 4.10 also compares our data to values measured by Johnson *et al.* [87]. They presented thermal resistance data that we converted to conductivity, scaled by the conductivity value in normal fluid  $^3\text{He}$  at the  $T_c$  for each pressure ( $(0.047 \frac{\text{W}}{\text{Km}}$  at 20 bar,  $(0.032 \frac{\text{W}}{\text{Km}}$  at 29.6 bar). It shows roughly the same order of magnitude as our data, but full correspondence between them and us is not expected due to different experimental conditions. Wellard *et al.* [88] studied the conductivity of superfluid  $^3\text{He}$  down to  $0.3T_c$  by observing a time delay of a heat pulse between two vibrating wires. This data was converted to diffusive conductivity by Einzel [85] as normalized to the normal fluid conductivity. The plateau in our measurements qualitatively matches with the diffusive conductivity.

Next, hydrodynamic conductivity can be evaluated from [90–92]

$$\kappa_h = \frac{d^2 T S_3^2}{32 \eta V_3^2}, \quad (4.5)$$

where  $d$  is the diameter of the liquid column,  $S_3$  the superfluid  $^3\text{He}$  entropy,  $V_3$  its molar volume, and  $\eta$  the viscosity. We used the normalized data given

by Ref. [85] with the normal fluid viscosity given by Ref. [48]

$$\eta = \left( \frac{1}{6.65(\text{T/mK})^2 + 12.8} + 10^{-5} \right) \text{Pas.} \quad (4.6)$$

Hydrodynamic conductivity alone is not enough to produce good agreement with our data, but when we sum it to the diffusive conductivity we gain some general resemblance. However, the local minimum at  $0.85T_c$  is not reproduced by it, but since the confidence bounds of our data are so loose, this combination still falls within them, until below  $0.6T_c$  our measured values are lower than the aforementioned sum.

Lastly, in Fig. 4.11 we compare the three routes of heat conduction in our system. The Kapitza resistance restricted heat flows (sinter and plain cell wall) were drawn by assuming that the nuclear stage was at zero temperature, while the heat flow through the connecting channel was calculated by integrating the multi-Gaussian function under the assumption that one end was at the zero-temperature limit. Even above the  $T_c$ , the sinter is in principle capable of sustaining larger heat flow than the plain cell wall, but since the flow through it is also restricted by the poor thermal conductivity of the normal fluid  $^3\text{He}$  in the connecting channel, heat flow through the cell wall becomes dominating contribution at sufficiently high temperature ( $\gtrsim 3T_c$ ). As we get closer to the  $T_c$ , the plain wall contribution

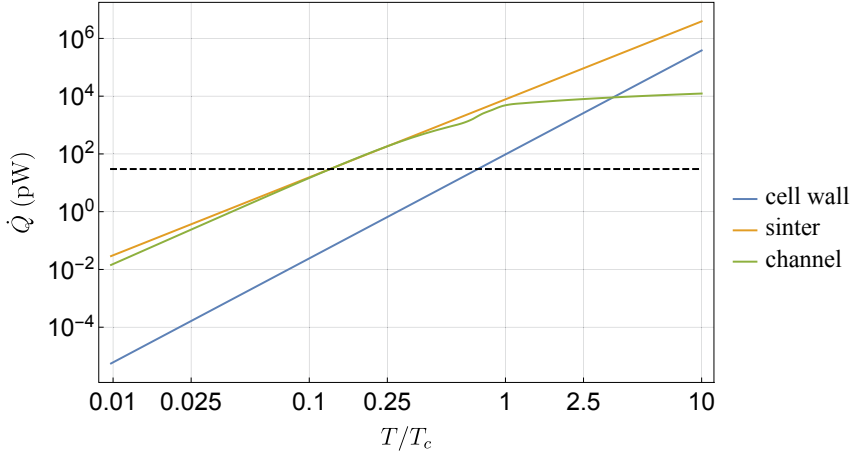


**Fig. 4.11** Maximum heat flows through the different conduction paths of our system as a function of temperature. The dashed black line indicates 30 pW reference point.

becomes rapidly negligible and the heat is mainly transferred through the sinter via the connecting channel. Then, at about  $0.15T_c$ , this path is able to sustain 30 pW heat flow, which is the order of magnitude of our heat leak, and thus the limit for the precooling.

## 4.4 Heat leaks

The final parameters to determine for our computational model are the flow dependent heat leak  $\dot{Q}_f$ , and the background external heat leak  $\dot{Q}_{\text{ext}}$ . When we know the thermal contact parameters and the quantities of different helium phases,  $\dot{Q}_{\text{ext}}$  can be deduced from the difference between temperatures  $T_L$  and  $T_{\text{NS}}$  the system approaches when undisturbed. We learned that we needed to have two different values for  $\dot{Q}_{\text{ext}}$ : one before the melt and the other after. The before-melting value was determined from  $T_L - T_{\text{NS}}$  at the end of precool, while the post-melting value was evaluated from the  $T_L - T_{\text{NS}}$  the system relaxed towards long after the melt was over.

We focus on 6 precool–melt–warm-up runs, like in Fig. 4.1, that met the following criteria: 1) the time between final crystal growth and start of the melt was sufficiently long to determine the amount mixture in the system based on the relaxation time, as well as the before-melting heat leak value, 2) the precooling temperature was low enough to allow us to attempt sub-100  $\mu\text{K}$  temperatures, 3) we were able to start and carry out the melting process without heat pulses caused by the operation of the superleak line, and 4) the post-melting follow-up time was long enough to enable us to determine the post-melting heat leak value and the nuclear stage temperature was stable during this time.

To compute  $T_L$  and  $T_V$  from Eqs. 3.13 and 3.14, we used the QTF determined temperature as the initial value for  $T_L$ , while the initial value for  $T_V$  was arrived at recursively starting from the mean value between  $T_L$  and  $T_{\text{NS}}$ . To approach the heat leak  $\dot{Q}_f$ , we assumed, for the moment, that it had a constant value through the entire melt, which was varied between different computational runs. The result is Fig. 4.12, where we compare measured  $T_L$  to computed values at various constant  $\dot{Q}_f$  during 6 different melts. The computed  $T_V$  is omitted from the figures for clarity.

We sought  $\dot{Q}_f$  that would result the best match between measured and computed post-melting warm-up periods. Its criterion was that the computed temperature should not cross the measured temperature at any

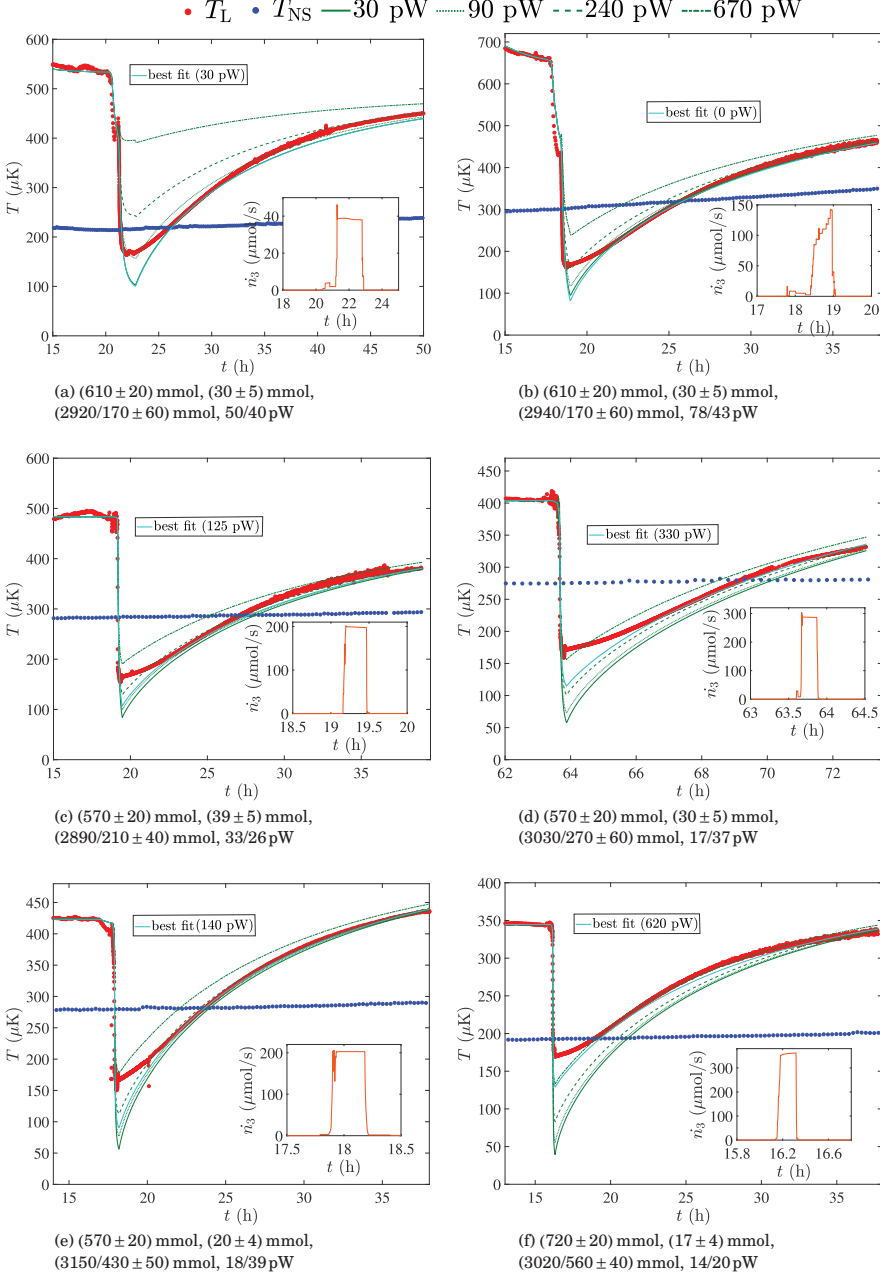


**Fig. 4.12** Measured nuclear stage temperature  $T_{NS}$ , and measured cell main volume temperature  $T_L$  next to the computed  $T_L$  values at various heat leaks  $\dot{Q}_f$  during melting shown in green. For each subfigure, the cyan line indicates the best fit to the post-melting warm-up period, while the inset shows the  $^3\text{He}$  phase-transfer rate during the melt. Below each subfigure: total  $^3\text{He}$  in the system,  $^3\text{He}$  in the mixture phase before melting, solid  $^4\text{He}$  before/after melting, and background heat leak before/after melting.  $t = 0$  is the time when the final solid growth was finished (full relaxation shown in Fig. 4.14)

point, but approach it asymptotically as soon as possible. When the maximum  $^3\text{He}$  phase-transfer rate  $\dot{n}_3$  (shown in the insets) was below about  $150 \mu\text{mol/s}$  no additional heat leak compared to  $\dot{Q}_{\text{ext}}$  is needed. But, as the rate exceeded  $200 \mu\text{mol/s}$ , we needed to increase it up to over  $600 \text{ pW}$  at  $\dot{n}_3 = 360 \mu\text{mol/s}$  in the computation to produce a reasonable correspondence to the measured behavior. From the "best fit" value, we then subtract the post-melting heat leak value to identify the heat leak that is left as the actual  $\dot{Q}_f$ . The dependence of this  $\dot{Q}_f$  from  $\dot{n}_3$  is shown in Fig. 4.13. The low melting rate points do not appear in the logarithmic plot, rather only part of their error bars are visible, and the two  $200 \mu\text{mol/s}$  datapoints fall right on top of each other. Fit to the dataset indicates third power dependence between the phase-transfer rate and the heat leak

$$\dot{Q}_f = 12.8 \left( \frac{\dot{n}_3}{\mu\text{mol/s}} \right)^3. \quad (4.7)$$

If  $\dot{Q}_f$  were a result of only viscous losses in the system, we would have expected  $\dot{n}_3^2$  dependence. But since that was not the case, we conclude that there is another component in the flow-rate dependent heat leak whose physical origin is not yet known.

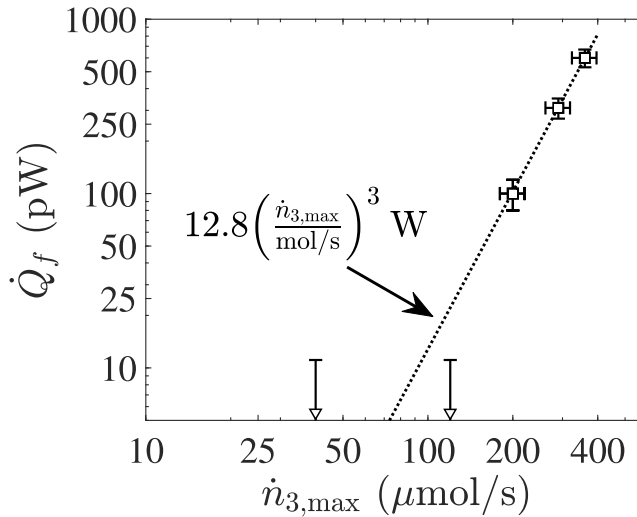


**Fig. 4.13** Heat leak  $\dot{Q}_f$  as a function of the maximum  $^3\text{He}$  phase-transfer rate  $\dot{n}_3$  determined from Fig. 4.12.

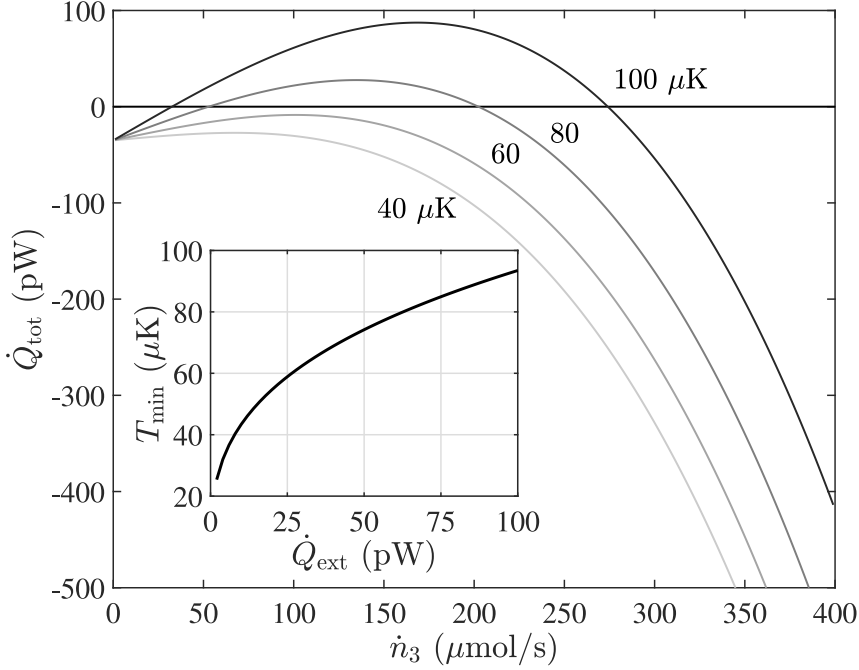


**Fig. 4.14** The total heat load in the system  $\dot{Q}_{\text{tot}} = \dot{Q}_{\text{melt}} - \dot{Q}_f - \dot{Q}_{\text{ext}}$  as a function of the  $^3\text{He}$  phase-transfer rate at several temperatures. Inset shows the dependence of the minimum temperature on the background heat leak  $\dot{Q}_{\text{ext}}$  at the optimal melting rate  $\dot{n}_{3,\text{opt}} = (0.048\dot{Q}_{\text{ext}}/1.22)^{1/3}$ .

Now that we know the heat leaks, we can estimate the minimum temperature obtainable at the optimal melting conditions. During the melt the temperature is so low that in Eq. (3.13) we can ignore the heat flow through the plain cell wall  $\dot{Q}_{\text{direct}}$  due to its massive Kapitza resistance, and  $\dot{Q}_{\text{tube}}$  since the  $^3\text{He}$  thermal conductivity in the channel is already small. Thus the total heat load to the cell main volume is approximately  $\dot{Q}_{\text{tot}} = \dot{Q}_{\text{melt}} - \dot{Q}_f - \dot{Q}_{\text{ext}}$ . When it is positive there is net cooling in the system. We used the average post-melting heat leak value for  $\dot{Q}_{\text{ext}} = 35$  pW from Fig. 4.12, and the known  $\dot{Q}_{\text{melt}}$  and  $\dot{Q}_f$  values to construct Fig. 4.14. The minimum temperature  $T_{\text{min}}$  at the optimal phase-transfer rate

$$\dot{n}_{3,\text{opt}} = \left( \frac{0.048\dot{Q}_{\text{ext}}}{1.22} \right)^{1/3} \quad (4.8)$$

is given by

$$T_{\min} = \sqrt{\frac{12.8\dot{n}_3^3 + \dot{Q}_{\text{ext}}}{109\dot{n}_{3,\text{opt}}}}, \quad (4.9)$$

which is shown in the inset.

Below that rate, the melting/mixing process is not enough to overcome the background heat leak, while above it the losses due to  $^4\text{He}$  flow become intolerably large. At  $\dot{Q}_{\text{ext}} = 35$  pW, the optimal phase-transfer rate  $\dot{n}_3 = 110$   $\mu\text{mol/s}$  (corresponding to  $\dot{n}_4 = 130$   $\mu\text{mol/s}$   $^4\text{He}$  extraction rate) results the minimum temperature 65  $\mu\text{K}$ .

## 4.5 Melts at higher temperatures

Now that the last unknown parameters of the computational model have been resolved, we can move on in our analysis. We begin with Fig. 4.15, where we take a look at several melts done at higher temperatures, where we could be sure that the  $^4\text{He}$  film effect did not yet affect the QTF thermometer behavior. At these temperatures the background heat leak  $\dot{Q}_{\text{ext}}$  of 0.1 pW order is again practically irrelevant, so we simply used the largest value from Fig. 4.18 for it always. In some cases we needed to adjust the amount of solid  $^4\text{He}$  the system had before the melt to produce a better match between measured and computed temperatures. This adjustment was at most 10% from our logged values, which was within the confidence bounds of the evaluated solid amount. Furthermore, the quality of the QTF data varies in these examples because we tried different measurement schemes in preparation for the lowest temperature runs. For instance, in Fig. 4.15b, we used alternating full-spectrum sweeps between the  $^3\text{He}$  QTF and the mixture QTF, when the latter was released from solid, while in Fig. 4.15c, we used the tracking mode with as small excitation as possible. In the measurement of Fig. 4.15d, we used the method that we ended up utilizing the most: full sweeps right until melting, tracking mode during the melt, and then full sweeps again after. Overall, the computed temperatures agree well with the measured values.

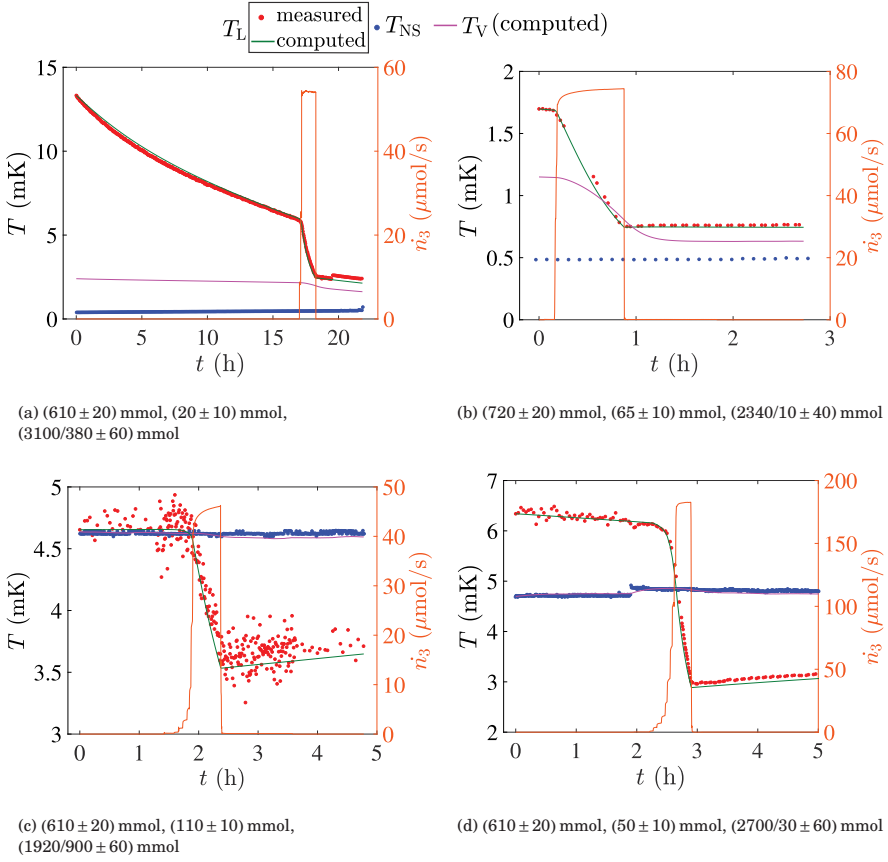


**Fig. 4.15** Left y-axis: measured nuclear stage temperature  $T_{NS}$  and measured cell main volume temperature  $T_L$ , with computed cell  $T_L$  and computed heat-exchanger volume temperature  $T_V$ . Right y-axis:  $^3\text{He}$  phase-transfer rate. Below each subfigure, from left to right, is: total  $^3\text{He}$  in the system,  $^3\text{He}$  in the mixture phase before melting, solid  $^4\text{He}$  before/after melting. Background heat leak was kept constant  $\dot{Q}_{\text{ext}} = 80$  pW here.

#### 4.5.1 Thermal gate operation

The purpose of the thermal gate was to isolate the main volume of the experimental cell from the heat-exchanger volume at the end of the precool in

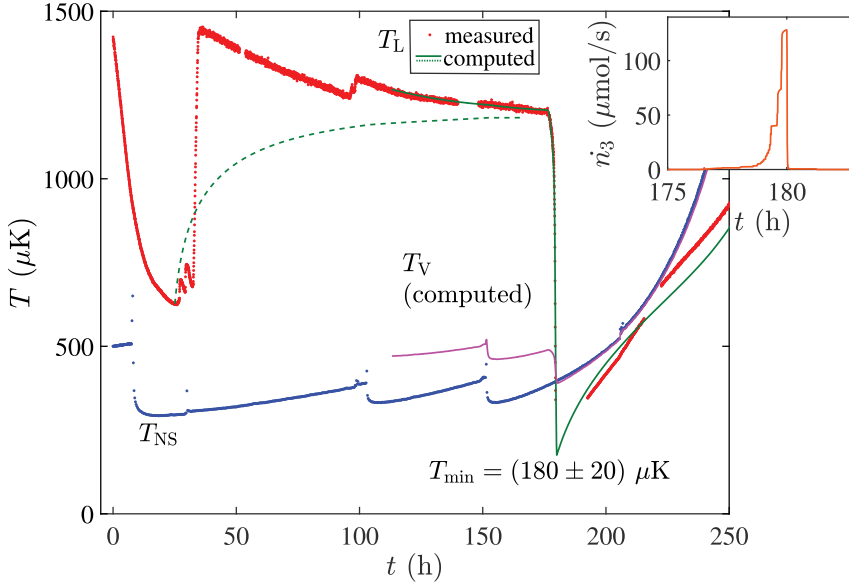


**Fig. 4.16** Measured nuclear stage temperature  $T_{NS}$  and measured cell main volume temperature  $T_L$ , with computed  $T_L$  and computed heat-exchanger volume temperature  $T_V$  during a thermal gate operation. Dashed green line shows the simulated  $T_L$  behavior at the closing of the TG, assuming no extra heating. The solid green line shows a simulation started from the point when TG was already completely closed (TG bellows at  $\sim 3$  bar). Total  $^3\text{He}$  ( $610 \pm 20$ ) mmol,  $^3\text{He}$  in mixture before the melt ( $19 \pm 5$ ) mmol, the amount of solid at the beginning/in the end ( $3110/250 \pm 60$ ) mmol, and heat leak before/after melt 47/27 pW. Inset shows the  $^3\text{He}$  phase-transfer rate during the melt.

an effort to eliminate all unnecessary heat leak sources during the melting. Unfortunately, we learned that the gate did not work as intended, which is demonstrated in Fig. 4.16.

From 0 to 25 h, the gate is open and the precool proceeds towards 500  $\mu\text{K}$  temperature, as expected. However, as soon as we start to increase the pressure in the miniature bellows system of the thermal gate to close it (cf. Section 2.3), heating spikes appear in the main volume that become more severe as the gate is further closed. We suspect that this behavior is caused by the friction between the bellows-operated stainless-steel ball and its saddle due to the roughness of the surfaces, or due to imperfect alignment. The volume of the miniature bellows is small, and it has two

lines connected to it: a normal line and a superleak line. It is possible that a sound mode can oscillate between the lines and cause mechanical vibrations that reach the stainless-steel ball, causing it to scrape the saddle making the friction heating worse. In an attempt to eliminate the oscillations in the lines, we filled the TG bellows with  $^3\text{He}$ – $^4\text{He}$  mixture to have the normal  $^3\text{He}$  component dampen the possible oscillations, but this had no effect to the observed heating.

Successful thermal gate operation would prevent heat leaks arriving to the heat-exchanger volume from reaching the main volume ( $\dot{Q}_{\text{extV}}$  in Eq. (3.14)), but would do nothing to the heat leaks that go directly to the main volume ( $\dot{Q}_{\text{ext}}$  in Eq. (3.13)). The dashed green line in Fig. 4.16 illustrates simulated main volume temperature behavior under the assumption that the thermal gate operation would not cause additional heating. As closing the gate effectively removes the  $\dot{Q}_{\text{tube}}$  contribution to Eq. (3.13), the heat is no longer removed from the main volume through the sinter in the heat-exchanger volume. Since the heat leak to the main volume is at the same time kept constant, temperature  $T_L$  must start to increase. The computed  $T_L$  does not reproduce the initial heat pulse, but the value the temperature relaxes towards is explained correctly by the computational model. This tells us that the majority of the heat leak to the main volume goes indeed directly there, and is not originated from the heat-exchanger volume. Thus we conclude that the closing the thermal gate, even under optimal conditions, would remove only a minuscule portion of the total heat leak going to the main volume, an advantage lost due to the excessive heating caused by the operation of TG.

### 4.5.2 Melting with the bellows system

The bellows system described in Section 2.4 provided an alternative method to carry out the melting procedure. With the help of the upper bellows, the volume of the lower bellows could be changed to accommodate the flow of  $^4\text{He}$  from the main volume of the experimental cell. Thus the 1 K section of the two-part superleak line could be blocked by solid  $^4\text{He}$ , as only the low-temperature section would now be needed. This way the bellows would isolate the experimental cell from anything above the low bellows temperature (dilution refrigerator temperature, 10 mK). However, this component of the experimental setup did not work as intended, either.

The first problem was that the bellows could not be moved enough to enable us to melt the entire  $^4\text{He}$  crystal. Usually, the maximum solid amount was slightly over 3 mol, and even by fully utilizing the bellows range of

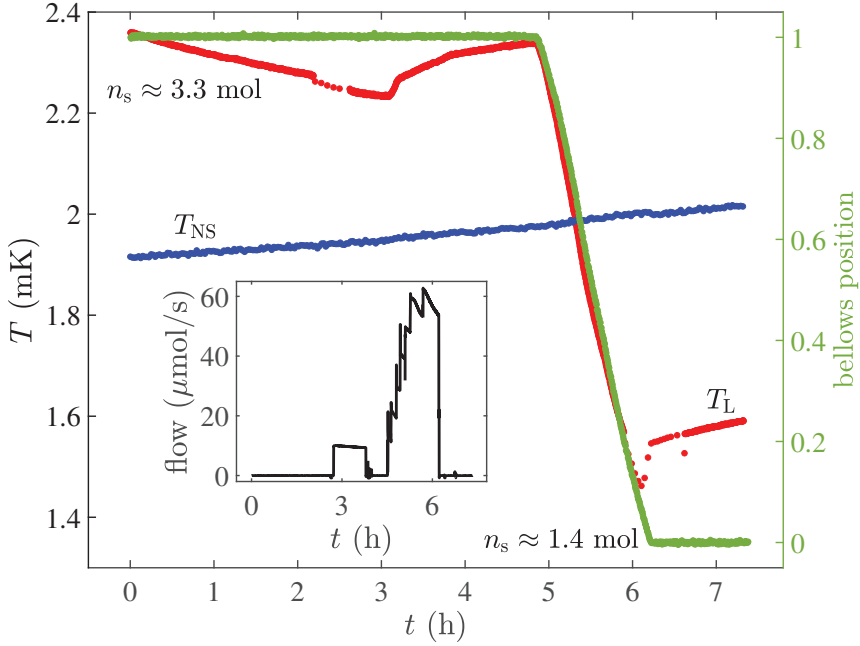


**Fig. 4.17** Left y-axis: measured nuclear stage temperature  $T_{NS}$  and measured cell main volume temperature  $T_L$  during a melting performed by the bellows system. Right y-axis: the position of the upper bellows in units where 1 is fully extended and 0 fully retracted. Inset shows the  $^4\text{He}$  extraction rate from the upper bellows.

motion, we could melt only 60% of it. Secondly, when the bellows was near the limits of its range, it caused heating in the main volume of the experimental cell, as is illustrated in Fig. 4.17. When we started to pump the upper bellows near 3 h point, at the rate shown in the inset, the main volume temperature immediately displayed signs of warming, even though the bellows was not even moving yet. As the bellows eventually started to move, some solid was successfully melted and the cell cooled down as it should have. But, when we reached the other end of the movement range, a second heating episode was observed.

The temperature here was of order 2 mK, and the heating was already a problem. Therefore, at sub-1 mK it would be completely detrimental to the experiment, since the cooling power of the melting process decreases as well. To keep excessive heating under control, the bellows should not

be allowed to reach either end of its movement capacity. But this would make the first problem even worse as we could melt even smaller portion of the solid than before. The third, and final problem is that by using the bellows we lose the ability to determine the amount of solid accurately, as we cannot directly measure the outgoing  $^4\text{He}$  flow from the cell anymore. We can, of course, convert the movement of the bellows to the extracted  $^4\text{He}$  amount, but it would introduce more error in the estimations. Since the drawbacks of the bellows operation outweighed its advantages, we focused our efforts on performing melts by pumping the superleak line from room temperature.

## 4.6 Lowest temperatures

Now, we return to the datasets presented in Fig. 4.12. We proceed by plugging in the determined  $\dot{Q}_f$  to the computational model and rerunning the simulations. The results are shown in Fig. 4.18, where the data is now shown starting from the end of the final solid growth, so that the relaxation towards lower temperatures is visible. The figure also shows the computed heat-exchanger temperature  $T_V$ , and the width of the mixture QTF as it emerges from solid at about the midpoint of the melt.

The lowest determined temperature was  $(90 \pm 20) \mu\text{K} \approx \frac{T_c}{(29 \pm 5)}$  in Fig. 4.18e with the maximum phase-transfer rate of about  $200 \mu\text{mol/s}$ . The confidence bounds include the uncertainties of the helium amounts in different phases, QTF temperature calibration, heat leaks, melting rate and the thermal parameters of the system. Out of these, the amount of initial mixture and the heat leaks were the most significant. The lowest temperatures in the other melts were above, or just below  $100 \mu\text{K}$ . If we compare the slow melting rate data of Fig. 4.18a to the high-rate data of Figs. 4.18d and 4.18f, we note that there is no notable improvement in the ultimate temperature, even if the latter two also had improved precooling conditions. This is due to the flow-dependent heat leak  $\dot{Q}_f$  canceling out the advantage gained by the lower precooling temperature.

When the mixture QTF emerges from solid, temperatures were at their lowest. The presented points are five-point moving averages of the measured values. In Figs. 4.18d and 4.18e the QTF was measured mostly in the tracking mode resulting in more datapoints. However, as we switched from the tracking to the full-spectrum sweeps there was usually a jump in the QTF response, as in Fig. 4.18d near 70 h point. We had to determine the tracking parameters several days before the melt when we were still

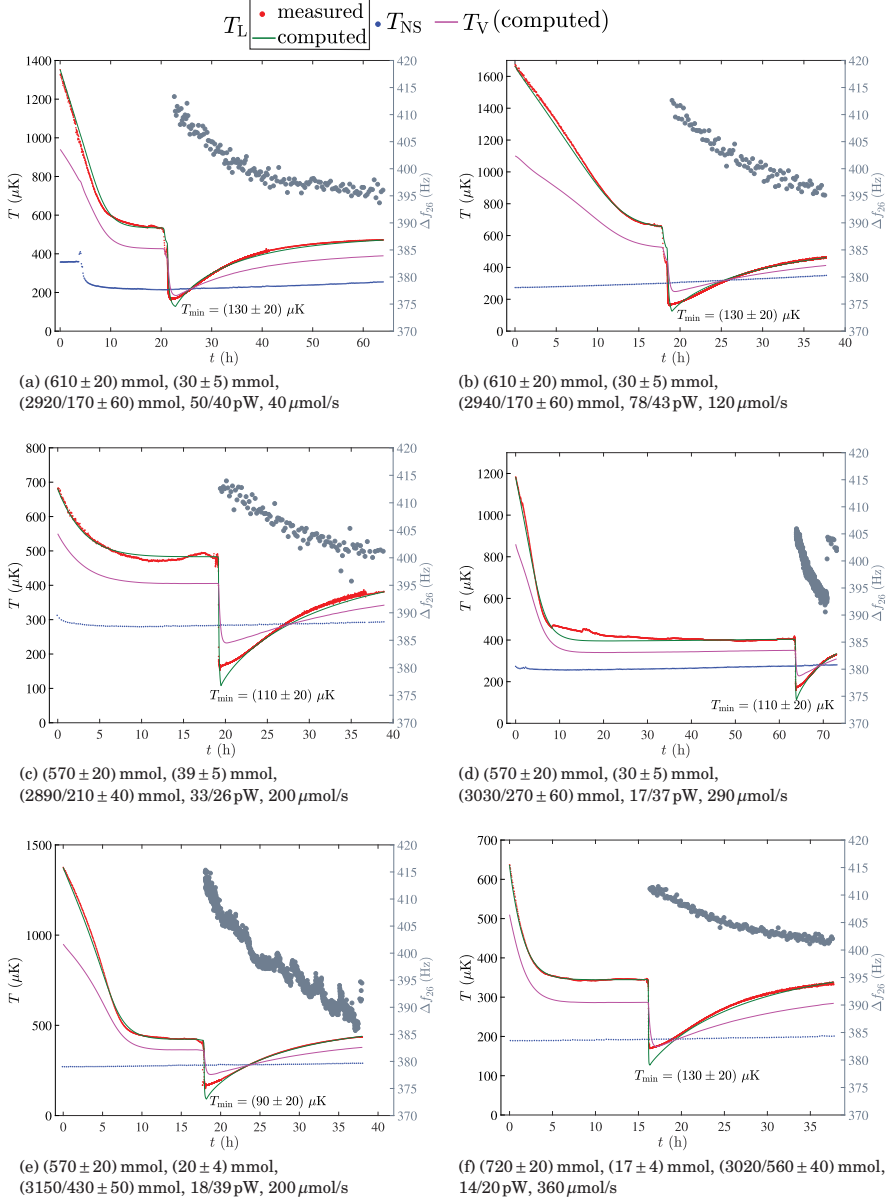


**Fig. 4.18** Left y-axis: Measured nuclear stage temperature  $T_{NS}$  and measured cell main volume temperature  $T_L$ , along with computed  $T_L$  and computed heat-exchanger volume temperature  $T_V$ . The lowest computed temperature is also written out. Right y-axis: resonance width of the mixture fork as it emerges from the solid  $^4\text{He}$  phase partway through the melt. At  $t = 0$  the solid growth was stopped. Below each subfigure: total  $^3\text{He}$  in the system,  $^3\text{He}$  in the mixture phase before melting, solid  $^4\text{He}$  before/after melting, background heat leak before/after melting, and the mean  $^3\text{He}$  phase-transfer rate  $\dot{n}_3$  (cf. Fig. 4.12).

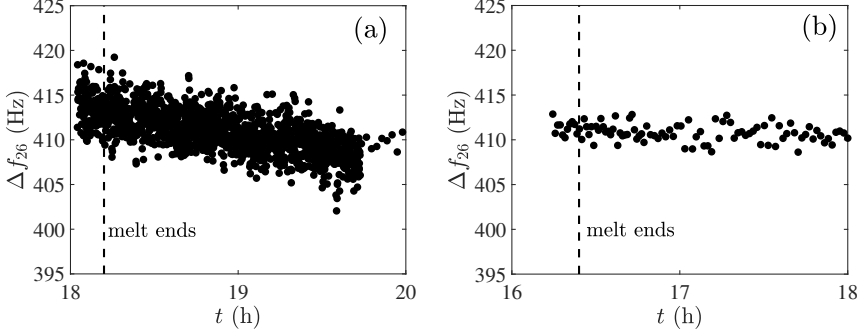


**Fig. 4.19** Close-up of the mixture QTF width during the coldest stages of the melts. (a) corresponds to Fig. 4.18e, and (b) to Fig. 4.18f.

growing the crystal and the mixture QTF was out of solid and measurable. It thus appears that they were no longer appropriate. In Figs. 4.18a-c, and 4.18f we used narrow full-spectrum sweeps for data gathering, which we now conclude was the most reliable method.

The mixture QTF response shows no indication of superfluid transition in the mixture phase. When it becomes measurable, the width initially remains almost constant and after the melting is over it starts to slowly decrease, as shown in the close-up Fig. 4.19. The points here are the raw measured data. The behavior is understandable as at the beginning the QTF is deep in the saturation region (cf. Fig. 4.2), but as the temperature increases enough after the melt, it begins to show shallow temperature dependence. Note, that the change in the mixture QTF width, over the span of several hours, was less than 5% from the maximum value. The slope in Fig. 4.19a can be partly due to the inaccurate tracking parameters, whereas Fig. 4.19b was measured in the full-frequency sweep mode. The unexciting mixture QTF response is in agreement with the determined lowest temperatures, as the mixture superfluidity is expected to occur only at around  $40 \mu\text{K}$  [16].

Next, in Fig. 4.20 we compare the entropy of the system to the ideal situation described in Section 3.1. We have used the computed temperature  $T_L$  from Fig. 4.18e as an example with the pure  $^3\text{He}$  and mixture curves taken from Fig. 3.1. Since there is mixture phase present in the before-melting state, the entropy deviates from the pure  $^3\text{He}$  curve. Then, during the melt the system initially follows the ideal adiabatic behavior going horizontally towards the mixture curve. But eventually below  $0.05T_c$ , heat

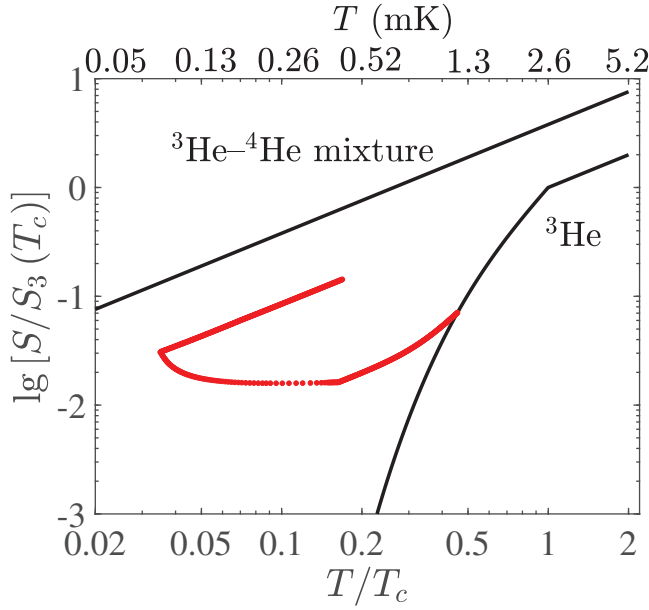


**Fig. 4.20** Entropy during the precool–melt–warm-up cycle scaled to the entropy of pure  $^3\text{He}$  at the  $T_c$  (cf. Fig. 4.18e and 4.1) with the entropies of pure  $^3\text{He}$  and saturated  $^3\text{He}$ – $^4\text{He}$  mixture, for reference.

leaks force it to bend towards elevated temperatures. At the end, there is still pure  $^3\text{He}$  phase present, meaning that the actual entropy stops short of the mixture-only curve, but runs parallel to it during the warm-up period. We can conclude that since during the precool the deviation from the pure  $^3\text{He}$  curve is already clear, the temperature our system reaches cooled by the nuclear stage was sufficiently low. As discussed in Section 3.1, when the deviation occurs, further precool decreases the theoretical final temperature only in proportion to the initial temperature, rather than exponentially. This is, of course, true with this specific mixture phase amount: if it could be reduced, further precooling would make sense. But, as we have seen, the heat leaks during the melt were the most critical factors limiting the ultimate temperature, and they would need to be addressed first.

#### 4.6.1 Simulations with altered melting conditions

Since we have a computational model of the experiment at our disposal, let us take a look at how changing certain parameters would affect the lowest

possible temperature obtainable in the melting process. We again focus on the melt presented in Fig. 4.18e, as it resulted the lowest temperature so far.

The results are shown in Fig. 4.21, where in Fig. 4.21a, we have halved or doubled the numerical prefactor of  $\dot{Q}_f$  in Eq. (4.7), resulting in approximately 10  $\mu\text{K}$  decrease, or 20  $\mu\text{K}$  increase in the lowest temperature, respectively. Then in Fig. 4.21b, we kept the original  $\dot{Q}_f$  but altered the phase-transfer rate  $\dot{n}_3$  while keeping the final solid amount constant. Thus, the simulated half-rate melt takes longer than the actual performed melt, and vice versa for the double-rate melt. Increasing  $\dot{n}_3$  has an adverse effect to the ultimate temperature as the  $\dot{n}_3^3$  dependence increases  $\dot{Q}_f$  drastically. As a matter of fact, had we halved  $\dot{n}_3$ , we could have ended up with about 10  $\mu\text{K}$  lower temperature. The additional line in Fig. 4.21b shows how a perfect operation of the thermal gate, *i.e.* no excess heating during its closing, would have affected the lowest temperature. Since the majority of the heat leak arrives directly to the main volume of the cell, closing off the heat-exchanger volume does not have a significant effect to the lowest temperature. Next, in Fig. 4.21c decreasing the amount of mixture before the melt should, in principle, result in improved performance. However, as long as the relatively large heat leak  $\dot{Q}_f$  is present, reduction in mixture amount would not cause significant improvement. On the other hand, increasing mixture amount would more clearly hinder the performance further, as expected.

Conversely, Figs. 4.21d-f demonstrate parameters that do not have much effect on the lowest temperature. The amount of mixture in the heat-exchanger volume (7 mmol) is comparable to the initial mixture in the main volume (20 mmol), but the two volumes are effectively isolated by the poor thermal conductivity of  $^3\text{He}$  in the connecting channel. Hence, the heat-exchanger mixture amount has only a minuscule effect on the performance of the melting process, as shown in Fig. 4.21d. Next, either changing the area of the sinter (Fig. 4.21e), or the diameter of the connecting channel (Fig. 4.21f) have similar effect: improved thermal contact results in a lower precooling temperature, but the advantage is lost during the melt since then there is also increased heat load coming from the nuclear stage to the experimental cell. The outcome stays the same with reduced thermal contact. In that case, the heat load during the melting period is decreased, but since the melt has to be started from a higher temperature, the effects cancel out each other in regards to the lowest obtainable temperature.

Thus, the most critical aspect in improving the performance is to take

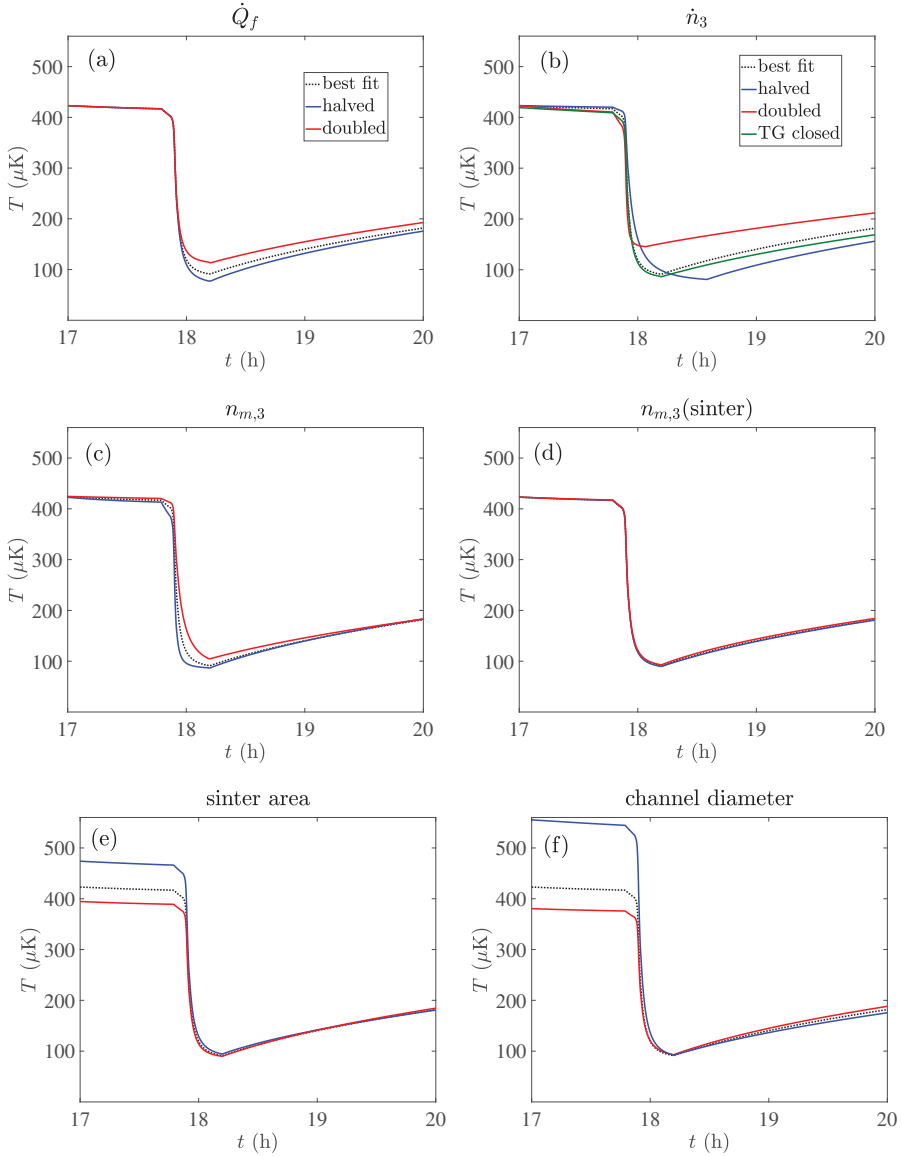


**Fig. 4.21** Simulated melting behavior with altered parameters compared to the calculation of Fig. 4.18e. Red lines correspond to two times larger parameter value, while in blue lines the value is halved. (a) Flow-rate dependent heat leak  $\dot{Q}_f$ , (b)  $^3\text{He}$  phase-transfer rate, plus the green line shows the melting if the thermal gate was closed at the beginning of the melt (without any additional heating), (c) the amount of  $^3\text{He}$  in the mixture phase before the melt, (d) the amount of  $^3\text{He}$  trapped as mixture in the pores of the sinter in the heat-exchanger volume, (e) surface area of the sinter (effectively  $2r_V$  and  $0.5r_V$  of Section 4.2.2), and (f) diameter of the channel connecting the cell main volume and the heat-exchanger volume.

care of the heat leaks. The most important is the background heat leak  $\dot{Q}_{\text{ext}}$ , and not the flow-dependent heat leak  $\dot{Q}_f$ , even if it currently was the most significant contribution to the total heat leak. If we were able to significantly reduce, or even completely remove,  $\dot{Q}_{\text{ext}}$ , we could melt the crystal at low enough rate for  $\dot{Q}_f$  to have negligible effect. Since at present,  $\dot{Q}_{\text{ext}}$  was still significant, we were forced to contend it by increasing the melting rate, which ended up causing further heating problems. But, in reality we can never completely get rid of  $\dot{Q}_{\text{ext}}$ , so a compromise between  $\dot{Q}_{\text{ext}}$  and  $\dot{Q}_f$  needs to be found. For example, it may be possible to reduce  $\dot{Q}_f$  by improving the performance of the superleak line. Then, if the heat leaks were under control, the next step is to reduce the amount of mixture in the state before the melt.



## Chapter 5

### Conclusions

The adiabatic melting method is a novel cooling technique that utilizes mixing of the two stable helium isotopes,  $^3\text{He}$  and  $^4\text{He}$  to absorb heat. As the cooling process takes place directly in the helium sample, the method circumvents thermal boundary resistance that conventionally limits the lowest temperatures achievable in helium by external cooling methods. The two isotopes are separated by increasing the pressure in the system to the crystallization pressure of  $^4\text{He}$  25.64 bar [11]. When this is done below 50 mK, we end up with a system of pure solid  $^4\text{He}$  and pure liquid  $^3\text{He}$ , and small, but thermodynamically significant, amount of remnant mixture. The system was precooled by a combination of four different cooling stages in sequence to achieve starting temperature of about 0.5 mK. Then, the solid phase was allowed to melt by extracting  $^4\text{He}$  from the system via a powder-filled capillary, or superleak, through which superfluid  $^4\text{He}$  is able to flow even at the bulk crystallization pressure. As the solid is melted, it releases liquid  $^4\text{He}$  which mixes with  $^3\text{He}$  to form a saturated mixture at 8.1% [46]  $^3\text{He}$  molar concentration, producing cooling. The initial system of mostly solid  $^4\text{He}$ –liquid superfluid  $^3\text{He}$  contains only a small amount of entropy, while the mixture phase contains relatively much more of it. Therefore, going adiabatically from phase-separated state to mixture state is only possible if the temperature of the system decreases. In theory, temperature can be lowered by more than a factor 1000, but in reality the remnant mixture in the initial state and external heat leaks limited this to about factor 5-7 in the presented work.

The experimental cell consisted of a large main volume (77 cm<sup>3</sup>) and a smaller sinter-filled heat-exchanger volume (5 cm<sup>3</sup> with 10 m<sup>2</sup> surface area) with a channel in between that could be restricted by a hydraulic valve, *i.e.* thermal gate. The gate was practically unusable because its

operation brought excessive heating to the main volume of the cell. Fortunately, the decreasing conductivity of superfluid  $^3\text{He}$  in the connecting channel alone was sufficient to isolate the main volume from the precooler during the coldest stages of the experimental runs.

Thermometry at such ultra-low temperatures is extremely challenging. Our main thermometer was a quartz tuning fork oscillator placed in the  $^3\text{He}$  phase. It worked down to about  $300\ \mu\text{K}$  (or  $0.2\ \text{Hz}$  full-resonance width at half-maximum), below which the presence of  $^4\text{He}$  film on its surface impaired its temperature sensitivity. Hence, we had to construct a computational model of the system to estimate the lowest achieved temperatures. For it, we studied various thermal parameters in our system that determined the flow of heat between the melting cell and the adiabatic nuclear demagnetization precooler. Our evaluated parameters were in line with the parameters obtained by others, although the data for the comparison of the superfluid  $^3\text{He}$  thermal conductivity was rather limited.

The lowest determined temperature was  $(90 \pm 20)\ \mu\text{K} \approx \frac{T_c}{(29 \pm 5)}$ , where  $T_c = 2.6\text{mK}$  [11]. This is still above the estimated superfluid transition temperature of  $^3\text{He}$  in the saturated mixture phase  $40\ \mu\text{K}$  [16]. The observations made with our second quartz tuning fork oscillator situated in the mixture agree with this: there was no indication of a new superfluid transition.

The main factor limiting the performance of the melting process was the background heat leak. To overcome it, we needed to increase the  $^3\text{He}$  phase-transfer rate from pure to mixture phase by melting the solid phase more rapidly, which turned out to cause excessive heating at the highest rates. We estimated that the optimal phase-transfer rate with our  $35\ \text{pW}$  background heat leak, would have been about  $100..150\ \mu\text{mol/s}$ . If the background heat leak can be reduced, the melting can be carried out slow enough that the flow-dependent contribution does not become detrimental. Beyond heat leaks, the next thing to take care of would be reducing the remnant mixture amount in the pre-melting system to decrease its entropy further.

We also suggest simplifying the setup further by removing the thermal gate, unless it can be improved to operate without excessive heating. It seems that the poor thermal conductivity of superfluid  $^3\text{He}$  in the channel connecting the main volume to the heat-exchanger volume can be enough to isolate them at the lowest temperatures. We would also suggest to remove the bellows system placed withing the dilution unit, as it did not perform as

intended. It could be replaced by a simpler buffer volume for the superleak line at the dilution refrigerator temperature (10 mK). We could also add a second buffer volume to the nuclear stage temperature (0.5 mK) to further isolate the main volume from any high-temperature parts.

The cell-side end of the superleak could be brought slightly higher to enable us to grow more solid  $^4\text{He}$ . We only need enough  $^3\text{He}$  in the main volume to saturate all  $^4\text{He}$  released from solid and to keep the thermometer quartz tuning fork always in pure  $^3\text{He}$ . We could also install a fork to the heat-exchanger volume to monitor its temperature, which could be used to procure additional information about the thermal conductivity of the connecting channel.

Another challenge is to come up with a thermometer that could be used to measure sub-100  $\mu\text{K}$  temperatures in liquid helium reliably. Mechanical oscillators do not cut it, since their minimum observable width seems to be determined by the  $^4\text{He}$  film covering them, rather than their intrinsic properties. Temperature could be measured by a nuclear magnetic resonance thermometer (PLM for example), which would have to be small in size and have a large surface area to have good thermalization with the liquid sample, which is opposed by the rapidly increasing Kapitza resistance. However, their biggest problem is the time the nuclear spin system needs to relax to reach proper thermal equilibrium with the lattice electrons (and thus with the helium sample). At 100  $\mu\text{K}$  it is of order 30 minutes, and becomes even longer at lower temperatures. Since the melting process can sustain the ultra-low temperatures only for a few minutes, we would simply not be able to gather data fast enough. A plausible solution would be to utilize the quadratic temperature dependence of the  $^4\text{He}$  crystallization pressure [11, 93, 94] in a pressure gauge. However, it would need to have an order  $10^{-9}$  bar resolution at 25 bar pressure, placing extreme demands on the stability and readout of the setup. One could perhaps also utilize a magnon BEC thermometer, that could, in principle, be used down to much lower temperatures than mechanical oscillators. Its operation is known to be viable [95–97], but it would require installing a non-metallic section to the main volume of our experimental cell to house the magnon sample and the surrounding NMR coils. This introduces more complexity, and possible heat leak sources to the arrangement but it can be an acceptable trade-off if the gain is a more reliable thermometer.

With the performance of the current setup, we would need the background heat leak to be below 10 pW to reach 40  $\mu\text{K}$  temperature. A chal-

lenging undertaking for sure, but nevertheless one that does not appear entirely impossible.

# List of symbols

symbol or abbreviation	description
BEC	Bose-Einstein Condensate
BCS	Bardeen–Cooper–Schrieffer
SVP	saturated vapor pressure
L	main volume of the experimental cell
V	heat-exchanger volume of the experimental cell
TG	thermal gate
SL	superleak line
QTF	quartz tuning fork
PLM	pulsed platinum NMR thermometer
$T$	temperature
$T_\lambda$	$^4\text{He}$ superfluid transition temperature
$T_c$	$^3\text{He}$ superfluid transition temperature
$T_{AB}$	$^3\text{He}$ superfluid A–B transition temperature
$T_F$	Fermi temperature
$T_{F,3}$	pure $^3\text{He}$ Fermi temperature
$T_{F,m}$	$^3\text{He}$ – $^4\text{He}$ mixture Fermi temperature
$T_{NS}$	nuclear stage temperature
$T_V$	cell main volume temperature
$T_L$	heat-exchanger volume temperature
$x$	molar concentration
$C$	heat capacity
$C_3$	pure $^3\text{He}$ heat capacity per mole of $^3\text{He}$

$C_{m,3}$	$^3\text{He}$ – $^4\text{He}$ mixture heat capacity per mole of $^3\text{He}$
$C_L$	cell main volume heat capacity per mole of $^3\text{He}$
$C_V$	heat-exchanger volume heat capacity per mole of $^3\text{He}$
$S$	entropy
$S_3$	pure $^3\text{He}$ entropy per mole of $^3\text{He}$
$S_{m,3}$	$^3\text{He}$ – $^4\text{He}$ mixture entropy per mole of $^3\text{He}$
$n$	amount of substance in moles
$n_3$	amount of $^3\text{He}$ in moles
$n_{m,3}$	amount of $^3\text{He}$ in $^3\text{He}$ – $^4\text{He}$ mixture in moles
$n_m$	amount of $^3\text{He}$ – $^4\text{He}$ mixture in moles
$n_s$	amount of solid $^4\text{He}$ in moles
$\dot{n}_3$	$^3\text{He}$ phase-transfer rate
$\dot{n}_4$	$^4\text{He}$ extraction rate
$R$	molar gas constant
$\hbar$	reduced Planck constant
$k_B$	Boltzmann constant
$N_A$	Avogadro constant
$\alpha$	BBP-parameter
$m$	mass
$m^*$	effective mass
$m_3$	$^3\text{He}$ atomic mass
$V_m$	liquid $^3\text{He}$ – $^4\text{He}$ mixture molar volume
$V_{4,l}$	liquid $^4\text{He}$ molar volume
$V_{4,s}$	solid $^4\text{He}$ molar volume
$V_3$	liquid $^3\text{He}$ molar volume
$\Delta_0$	superfluid $^3\text{He}$ energy gap
$R_K$	Kapitza resistance
$R_0$	Kapitza coefficient
$A$	surface area
$p$	Kapitza exponent
$r$	alternate Kapitza coefficient ( $r = A/R_0$ )
$p_L$	plain cell wall Kapitza exponent
$p_V$	sinter Kapitza exponent

$r_L$	plain cell wall Kapitza coefficient
$r_V$	sinter Kapitza coefficient
$R_T$	thermal resistance of liquid column
$l$	length
$d$	diameter
$D$	tube dimension parameter $D = \pi d^2/(4l)$
$\kappa$	thermal conductivity
$\kappa_0$	normal fluid $^3\text{He}$ thermal conductivity
$\kappa_1$	superfluid $^3\text{He}$ thermal conductivity
$\dot{Q}_{\text{melt}}$	cooling power of the melting process
$\dot{Q}_{\text{ext}}$	background heat leak
$\dot{Q}_f$	flow-rate dependent heat leak
$\dot{Q}_{\text{direct}}$	heat flow through the plain cell wall
$\dot{Q}_{\text{sinter}}$	heat flow through the sinter in the heat-exchanger volume
$\dot{Q}_{\text{tube}}$	heat flow through the connecting channel
$f_{32}$	QTF resonance frequency
$\Delta f_{32}$	QTF resonance full-width at half-maximum
$\Delta f_b$	QTF width at ballistic crossover
$\Delta f_0$	QTF residual width
$\Delta f_{AB}$	QTF width at $T_{AB}$
$f_{\text{vac}}$	QTF vacuum resonance frequency
$\rho$	$^3\text{He}$ density
$\eta$	$^3\text{He}$ viscosity



## References

- [1] H. Kamerlingh Onnes, Proc. KNAW. **11**, 168 (1909).
- [2] D. van Delft and P. Kes, Physics Today **63**, 38 (2010).
- [3] S. N. Bose, Zeit. Phys. **26**, 178 (1924).
- [4] A. Einstein, Sitzungsberichte der Preussischen Akademie der Wissenschaften **1** (1925).
- [5] J. Bardeen, L. N. Cooper, and J. R. Schrieffer, Phys. Rev. **108**, 1175 (1957).
- [6] E. R. Dobbs, *Helium Three (International Series of Monographs on Physics)* (Oxford University Press, 2001), ISBN 0198506406.
- [7] J. Rysti, Ph.D. thesis, Aalto University (2013).
- [8] S. Balibar, T. Mizusaki, and Y. Sasaki, J. Low Temp. Phys. **120**, 293 (2000).
- [9] S. Balibar, J. Low Temp. Phys. **129**, 363 (2002).
- [10] C. Pantalei, X. Rojas, D. O. Edwards, H. J. Maris, and S. Balibar, J. Low Temp. Phys. **159**, 452 (2010).
- [11] E. Pentti, J. Tuoriniemi, A. Salmela, and A. Sebedash, J. Low Temp. Phys. **146**, 71 (2007).
- [12] C. A. Ebner, Ph.D. thesis, University of Illinois (1967).
- [13] J. Bardeen, G. Baym, and D. Pines, Phys. Rev. **156**, 207 (1967).
- [14] M. K. Al-Sugheir, H. B. Ghassib, and B. R. Joudeh, Int. J. Mod. Phys. B **20**, 2491 (2006).

- [15] A. Sandouqa, B. Joudeh, M. Al-Sugheir, and H. Ghassib, *Acta Phys. Pol. A* **119**, 807 (2011).
- [16] J. Rysti, J. T. Tuoriniemi, and A. J. Salmela, *Phys. Rev. B* **85**, 134529/1 (2012).
- [17] J. J. Kinnunen and G. M. Bruun, *Phys. Rev. A* **91** (2015).
- [18] F. Chevy, *Phys. Rev. A* **91** (2015).
- [19] M. Delehay, S. Laurent, I. Ferrier-Barbut, S. Jin, F. Chevy, and C. Salomon, *Phys. Rev. Lett.* **115** (2015).
- [20] M. Abad, A. Recati, S. Stringari, and F. Chevy, *Eur. Phys. J. D* **69** (2015).
- [21] R. Onofrio, *Physics-Uspekhi* **59**, 1129 (2016).
- [22] I. Ferrier-Barbut, M. Delehay, S. Laurent, A. T. Grier, M. Pierce, B. S. Rem, F. Chevy, and C. Salomon, *Science* **345**, 1035 (2014).
- [23] R. Roy, A. Green, R. Bowler, and S. Gupta, *Phys. Rev. Lett.* **118**, 055301 (2017).
- [24] I. Pomeranchuk, *Zh. Eksp. Teor. Fiz* **20**, 919 (1950).
- [25] Y. D. Anufriev, *JETP* **1**, 155 (1965).
- [26] D. D. Osheroff, R. C. Richardson, and D. M. Lee, *Phys. Rev. Lett.* **28**, 885 (1972).
- [27] D. D. Osheroff, W. J. Gully, R. C. Richardson, and D. M. Lee, *Phys. Rev. Lett.* **29**, 920 (1972).
- [28] G. H. Oh, Y. Ishimoto, T. Kawae, M. Nakagawa, O. Ishikawa, T. Hata, T. Kodama, and S. Ikehata, *J. Low Temp. Phys.* **95**, 525 (1994).
- [29] P. L. Kapitza, *Physical Review* **60**, 354 (1941).
- [30] A. P. Sebedash, *JETP Lett.* **65**, 276 (1997).
- [31] A. Sebedash, *Physica B: Condensed Matter* **284-288**, 325 (2000).
- [32] J. Tuoriniemi, J. Martikainen, E. Pentti, A. Sebedash, S. Boldarev, and G. Pickett, *J. Low Temp. Phys.* **129**, 531 (2002).

- [33] E. M. M. Pentti, Ph.D. thesis, Helsinki University of Technology (2009).
- [34] A. Salmela, Ph.D. thesis, Aalto University (2012).
- [35] A. P. Sebedash, J. T. Tuoriniemi, S. T. Boldarev, E. M. M. Pentti, and A. J. Salmela, *J. Low Temp. Phys.* **148**, 725 (2007).
- [36] J. Rysti and J. Tuoriniemi, *J. Low Temp. Phys.* **171**, 273 (2012).
- [37] J. T. Tuoriniemi, J. Rysti, A. J. Salmela, and M. S. Manninen, *J. Phys.: Conf. Series* **400**, 1 (2012).
- [38] T. Knuuttila, Ph.D. thesis, Helsinki University of Technology (2000).
- [39] F. Pobell, *Matter and Methods at Low Temperatures* (Springer, , 2007), 3rd ed.
- [40] O. V. Lounasmaa, *Experimental Principles and Methods Below 1K* (Academic Press Inc. (London), , 1974).
- [41] K. R. Atkins, *Phys. Rev.* **113**, 962 (1959).
- [42] Y. D. Anufriev, V. N. Lopatik, and A. P. Sebedash, *JETP Lett.* **37**, 45 (1983).
- [43] V. N. Lopatik, *Sov. Phys. JETP* **59**, 284 (1984).
- [44] R. Blaauwgeers, M. Blazkova, M. Človečko, V. B. Eltsov, R. de Graaf, J. Hosio, M. Krusius, D. Schmoranz, W. Schoepe, L. Skrbek, et al., *J. Low Temp. Phys.* **146**, 537 (2007).
- [45] A. P. Sebedash, J. T. Tuoriniemi, E. M. M. Pentti, and A. J. Salmela, *J. Low Temp. Phys.* **150**, 181 (2008).
- [46] E. M. Pentti, J. T. Tuoriniemi, A. J. Salmela, and A. P. Sebedash, *Phys. Rev. B* **78**, 064509 (2008).
- [47] D. I. Bradley, M. J. Fear, S. N. Fisher, A. M. Guénault, R. P. Haley, C. R. Lawson, P. V. E. McClintock, G. R. Pickett, R. Schanen, V. Tsepelin, et al., *J. Low Temp. Phys.* **156**, 116 (2009).
- [48] E. Pentti, J. Rysti, A. Salmela, A. Sebedash, and J. Tuoriniemi, *J. Low Temp. Phys.* **165**, 132 (2011).
- [49] I. Todoshchenko, J.-P. Kaikkonen, R. Blaauwgeers, P. J. Hakonen, and A. Savin, *Rev. Sci. Instrum.* **85**, 085106 (2014).

- [50] T. Virtanen, Ph.D. thesis, University of Oulu, Department of Physics, Finland (2011).
- [51] A. M. Guénault, R. P. Haley, S. Kafanov, M. T. Noble, G. R. Pickett, M. Poole, R. Schanen, V. Tsepelin, J. Vonka, T. Wilcox, et al., *Physical Review B* **100** (2019).
- [52] L. Tisza, *Nature* **141**, 913 (1938).
- [53] L. Tisza, *Phys. Rev.* **72**, 838 (1947).
- [54] L. Landau, *Phys. Rev.* **60**, 356 (1941).
- [55] I. M. Khalatnikov, *An Introduction to the Theory of Superfluidity* (Westview Press, , 2000).
- [56] P. Brusov, J. M. Parpia, P. Brusov, and G. Lawes, *Phys. Rev. B* **63**, 140507(R) (2001).
- [57] A. J. Salmela, J. T. Tuoriniemi, E. M. M. Pentti, A. P. Sebedash, and J. Rysti, *J. Phys.: Conf. Series* **150**, 012040 (2009).
- [58] A. Salmela, J. Tuoriniemi, and J. Rysti, *J. Low Temp. Phys.* **162**, 678 (2010).
- [59] J. Rysti and J. Tuoriniemi, *J. Low Temp. Phys.* **177**, 133 (2014).
- [60] S. Balibar, H. Alles, and A. Y. Parshin, *Rev. Mod. Phys.* **77**, 317 (2005).
- [61] T. A. Alvesalo, T. Haavasoja, and M. T. Manninen, *J. Low Temp. Phys.* **45**, 373 (1981).
- [62] D. S. Greywall, *Phys. Rev. B* **27**, 2747 (1983).
- [63] E. Tanaka, K. Hatakeyama, S. Noma, and T. Satoh, *Cryogenics* **40**, 365 (2000).
- [64] G. E. Watson, J. D. Reppy, and R. C. Richardson, *Phys. Rev.* **188**, 384 (1969).
- [65] M. Kollar and D. Vollhardt, *Phys. Rev. B* **61**, 15347 (2000).
- [66] A. Driessen, E. van der Poll, and I. F. Silvera, *Phys. Rev. B* **33**, 3269 (1986).
- [67] D. S. Greywall, *Phys. Rev. B* **33**, 7520 (1986).

- [68] J. Serene and D. Rainer, *Phys. Rep.* **101**, 221 (1983).
- [69] A. P. J. Voncken, D. Riese, L. P. Roobol, R. Konig, and F. Pobell, *J. Low Temp. Phys.* **105**, 93 (1996).
- [70] P. Busch, S. Cheston, and D. Greywall, *Cryogenics* **24**, 445 (1984).
- [71] C. A. M. Castelijns, K. F. Coates, A. M. Guénault, S. G. Mussett, and G. R. Pickett, *Phys. Rev. Lett.* **55**, 2021 (1985).
- [72] D. S. Greywall, *Phys. Rev. B* **29**, 4933 (1984).
- [73] T. H. Virtanen and E. V. Thuneberg, *Phys. Rev. B* **83** (2011).
- [74] S. Autti, V. Dmitriev, J. Mäkinen, A. Soldatov, G. Volovik, A. Yudin, V. Zavjalov, and V. Eltsov, *Phys. Rev. Lett.* **117** (2016).
- [75] V. Dmitriev, A. Soldatov, and A. Yudin, *Phys. Rev. Lett.* **120** (2018).
- [76] V. P. Peshkov, *JETP Lett.* **21**, 162 (1975).
- [77] G. Agnolet, D. F. McQueeney, and J. D. Reppy, *Phys. Rev. B* **39**, 8934 (1989).
- [78] D. Kim, M. Nakagawa, O. Ishikawa, T. Hata, and T. Kodama, *Phys. Rev. Lett.* **71**, 1581 (1993).
- [79] S. T. Boldarev, R. B. Gusev, S. I. Danilin, and A. Y. Parshin, *Instrum. Exp. Tech.* **54**, 740 (2011).
- [80] S. Murakawa, M. Wasai, K. Akiyama, Y. Wada, Y. Tamura, R. Nomura, and Y. Okuda, *Phys. Rev. Lett.* **108** (2012).
- [81] A. I. Ahonen, O. V. Lounasmaa, and M. C. Veuro, *J. Phys. Colloq.* **39**, C6 (1978).
- [82] T. J. Greytak, R. T. Johnson, D. N. Paulson, and J. C. Wheatley, *Phys. Rev. Lett.* **31**, 452 (1973).
- [83] M. Dorfle, H. Brand, and R. Graham, *J. Phys. C* **13**, 3337 (1980).
- [84] J. Hara, *J. Low Temp. Phys.* **43**, 533 (1981).
- [85] D. Einzel, *J. Low Temp. Phys.* **54**, 427 (1984).
- [86] R. Afzali and N. Ebrahimian, *J. Phys.: Cond. Matt.* **17**, 4441 (2005).

- [87] R. T. Johnson, R. L. Kleinberg, R. A. Webb, and J. C. Wheatley, *J. Low Temp. Phys.* **18**, 501 (1975).
- [88] N. Wellard, P. Alexander, H. Hall, and J. Hook, *Physica B+C* **109-110**, 2096 (1982).
- [89] S. Yip, *Phys. Rev. B* **32**, 2915 (1985).
- [90] F. London and P. R. Zilsel, *Phys. Rev.* **74**, 1148 (1948).
- [91] C. J. Pethick, H. Smith, and P. Bhattacharyya, *Phys. Rev. Lett.* **34**, 643 (1975).
- [92] C. J. Pethick, H. Smith, and P. Bhattacharyya, *Phys. Rev. B* **15**, 3384 (1977).
- [93] J. Rysti, M. S. Manninen, and J. Tuoriniemi, *J. Low Temp. Phys.* **175**, 739 (2014).
- [94] A. Sebedash, J. T. Tuoriniemi, S. Boldarev, E. M. Pentti, and A. J. Salmela, *AIP Conf. Proc.* (2006).
- [95] S. Autti, Y. M. Bunkov, V. B. Eltsov, P. J. Heikkinen, J. J. Hosio, P. Hunger, M. Krusius, and G. E. Volovik, *Phys. Rev. Lett.* **108** (2012).
- [96] P. J. Heikkinen, S. Autti, V. B. Eltsov, J. J. Hosio, M. Krusius, and V. V. Zavjalov, *J. Low Temp. Phys.* **175**, 3 (2013).
- [97] P. J. Heikkinen, Ph.D. thesis, Aalto University (2016).



ISBN 978-952-60-8992-8 (printed)  
ISBN 978-952-60-8993-5 (pdf)  
ISSN 1799-4934 (printed)  
ISSN 1799-4942 (pdf)

**Aalto University**  
**School of Science**  
Department of Applied Physics  
[www.aalto.fi](http://www.aalto.fi)

**BUSINESS +  
ECONOMY**

**ART +  
DESIGN +  
ARCHITECTURE**

**SCIENCE +  
TECHNOLOGY**

**CROSSOVER**

**DOCTORAL  
DISSERTATIONS**